**FACULTY
OF MATHEMATICS
AND PHYSICS
Charles University**

MASTER THESIS

Bc. Jakub Maruška

Variability of the Martian ionosphere

Department of surface and plasma science

Supervisor of the master thesis: doc. RNDr. František Němec, Ph.D.

Study programme: Physics

Specialization: Surface and plasma physics

Prague 2021

Title: Variability of the Martian ionosphere

Author: Bc. Jakub Maruška

Department / Institute: Department of Surface and Plasma Science

Supervisor of the master thesis: doc. RNDr. František Němec, Ph.D.

Abstract: Historically, studying the Martian ionosphere has been difficult due to the lack of dedicated instruments for electron density measurements in the orbit of Mars. However, since 2005, radio occultation measurements have been supplemented by Mars Express MARSIS remote sounder data and, more recently, by data from the MAVEN LPW Langmuir probe since 2014. The ionosphere of Mars is an interesting system, because Mars as one of the two solar system planetary bodies without an intrinsic magnetic field has highly localised crustal magnetic fields. The Chapman model describes the main layer of the ionosphere surprisingly well. Nevertheless, the crustal magnetic fields and other parameters potentially influence the ionosphere formation and topology. Combining the recent vast electron density data set, the Mars Global Surveyor crustal magnetic field map, and F10.7 solar radio flux measurements carried out at the Earth, a detailed study of the influence of these parameters can be conducted. To study the influence of these parameters as well as solar zenith angle on electron densities in the Martian ionosphere, we study magnitude of deviations from the established Chapman model. Furthermore, we use the Kolmogorov's 5/3 power law to investigate a possible dependence of its parameters characterising power and dissipation of the fluctuations on relevant parameters.

Keywords: Mars, ionosphere, fluctuations, Mars Express, Chapman model

Contents

Introduction

Mars, as our closest neighbour, has long been an interesting subject for study. Missions to Mars began already in the 1960s with flyby missions, followed by several orbiters and two Viking landers in 1970s. At the break of the century, Mars Global Surveyor (MGS) mission established that Mars, while lacking strong intrinsic magnetic field, has localised remnant magnetic fields in its crust with magnitudes up to about 1600nT. An additional global magnetic field is induced by ionospheric currents due to the interaction with the solar wind. This combination makes Mars an interesting body to study since its ionosphere is probably controlled by both induced and crustal fields.

Radio occultation measurements by MGS provided data on electron density profiles at solar zenith angles (SZAs) from 44° to 136°. More recently, the Mars Express and MAVEN orbiters, now in orbit around Mars, collect valuable ionospheric data. Mars Advanced Radar for Subsurface and Ionosphere Sounding (MARSIS) on board Mars Express remotely measures altitude dependent profiles of electron density. MAVEN, on the other hand, routinely dips into the Martian ionosphere down to altitudes of peak electron densities and measures local densities using its Langmuir Probe and Waves (LPW) instrument.

This thesis is focused on studying factors influencing the variability of electron densities in the Martian ionosphere. We mainly use data from Mars Express and to a lesser degree data from the MAVEN spacecraft. To inspect the overall ionospheric situation and the effects of magnetic fields, we calculate mean electron densities with respect to the altitude of measurement and SZA, and we compare the results obtained for various magnetic field strengths and orientations.

Close to the peak altitude, the Mars ionosphere has been shown to correspond well to the Chapman model [1]. We investigate peak electron density differences from the expected SZA dependence. Additionally, the variability of electron densities in time or space can be studied using Fourier transform (FT). We calculate the respective spectra and study their dependence on relevant controlling parameters.

1. Theoretical Background

1.1   Solar wind interaction with an unmagnetized, atmospheric body

An unmagnetized body with an ionized atmosphere (ionosphere) poses more complicated obstacle to a plasma flow than an unmagnetized body without the atmosphere. Ionized particles in the atmosphere make it conductive; time-varying magnetic fields therefore induce currents that, in turn, produce opposing magnetic fields.
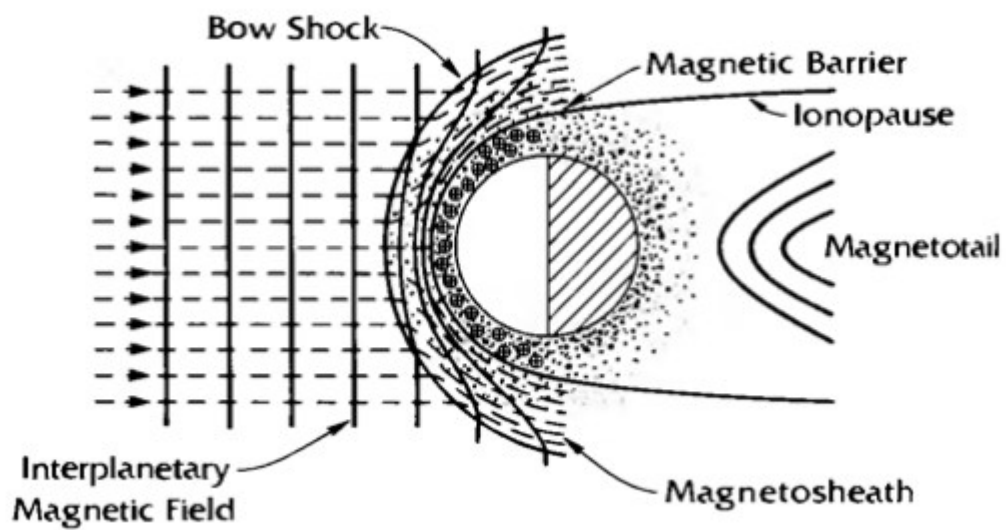
Figure 1 - Illustration of the interaction of flowing plasma with frozen-in magnetic field, like solar wind, with an unmagnetized body with an ionized atmosphere. (Adopted from [2].)

Space around such a body can be divided into regions according to different characteristics of plasma (see Figure 1). The first region is the interplanetary space, in which the pristine solar wind flows unperturbed by the obstacle ahead. The plasma there moves at supermagnetosonic velocities and the interplanetary magnetic field (IMF) is frozen in the plasma. The second region is the magnetosheath, where the plasma is slower and hotter, and the magnetic field is stronger than in the pristine solar wind. Last region is the induced magnetosphere and ionosphere, where the solar wind plasma and magnetic field do not have access and the plasma is produced from the neutral atmosphere around the body.

The individual plasma regions are separated by comparatively thin boundaries, across which the plasma properties change abruptly. The first boundary encountered

by the solar wind is a layer where the solar wind plasma is slowed down to submagnetosonic speeds and a part of its kinetic energy is converted into the thermal energy. This boundary is called bow shock and it separates the interplanetary space and the magnetosheath [2]. The magnetic field magnitude increases substantially at a layer called magnetic pile-up boundary (MPB), which separates the magnetosheath from the induced magnetosphere/ionosphere. The incident magnetic field does not penetrate this boundary due to the currents induced in the ionosphere, which create a cancelling field opposing the changes in the incoming field. The solar wind plasma flow cannot continue through the magnetic pile-up boundary, since the magnetic field is frozen in the plasma, and the flow is therefore diverted around the obstacle. The magnetic pile-up boundary can be thus viewed as a barrier between the regions of interplanetary and ionospheric plasma [3].

1.2   Solar wind interaction with Mars

In case of planets with significant global magnetic field, the ionosphere region is usually well shielded from the interplanetary space by the planetary magnetic field. However, that is not the case for Mars, whose magnetic dynamo is long gone and whose interaction with the solar wind is mainly ionospheric-atmospheric [4]. The thermal ionospheric pressure is not strong enough to hold off average solar wind, which has led many to believe that either intrinsic or induced magnetic field must be present to balance the dynamic pressure of the solar wind. Mars Global Surveyor (MGS) measurements finally showed that Mars does not have an intrinsic magnetic field. It thus presents an obstacle to the solar wind flow in a way similar to other unmagnetized atmospheric bodies like Venus [5]. Since Mars lacks substantial intrinsic magnetic field and the ionospheric thermal pressure is insufficient to hold off the solar wind dynamic pressure, the magnetic field from the magnetosheath penetrates into the ionosphere. This field then adds to the ambient pressure in the ionosphere and balances out the solar wind dynamic pressure.

It is reasonable to expect that the overall situation is essentially the same as the general scheme described in the previous subchapter (see Figure 2). Both the bow shock and MPB (sometimes also called planetopause) are routinely identified in spacecraft data [3]. An additional boundary, corresponding to an abrupt significant decrease of the ionospheric densities at high altitudes, so-called ionopause, is often

identifiable planetward of the MPB [6]. The positions of bow shock and MBP at Mars are influenced by variations in solar extreme ultraviolet (EUV) flux and, albeit possibly to a lesser extent, also by the changes of the solar wind dynamic pressure. During the periods of high solar activity and/or lower Sun-Mars distances, the solar wind dynamic pressure tends to be higher. However, at the same time, the higher EUV flux produces more ions in the ionosphere. The conductivity of the ionosphere therefore increases, which tends to move the boundaries farther from the planet [3].
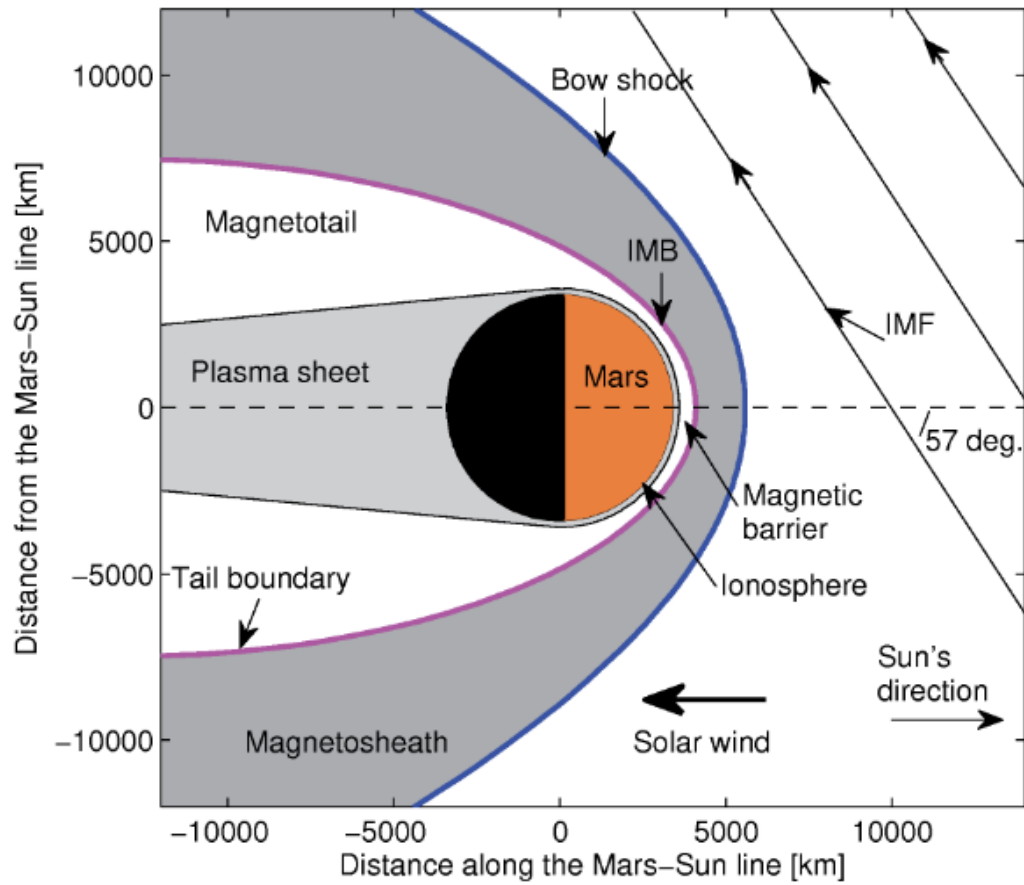
Figure 2 - Solar wind interaction with Mars. (Adopted from [7].)

1.3   Formation of the Martian ionosphere

The Martian ionosphere, same as others, is strongly dependent on the composition of the neutral atmosphere, from which it is produced. Prior to the MAVEN mission, the measured composition data were very scarce, coming essentially only from the Viking 1 and 2 landers. These landers measured the composition during their descent to the surface. Vertical profiles of CO_2, N_2, Ar, CO, and O_2 were measured [8] (see Figure 3). Although the instruments onboard the

Viking landers were incapable of measuring O, the UV remote sensing data and ionospheric composition data suggest that O densities are significant in the upper atmosphere [9].
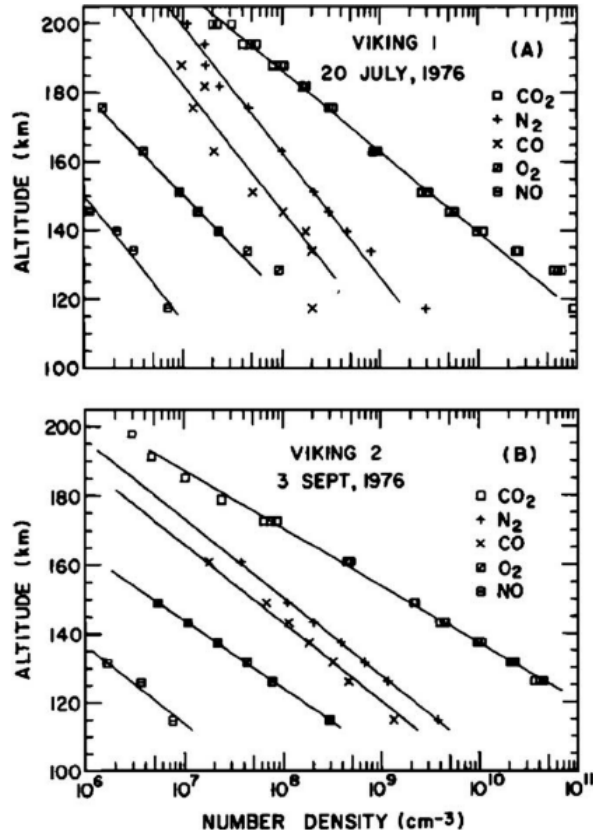
Figure 3 - Vertical profiles of individual species in the Martian atmosphere measured by the Viking 1 and 2 landers. (Adopted from [8].)

Primary source of plasma in the ionosphere is photoionization of CO2 by solar radiation at wavelengths shorter than 90 nm [10]. Photoionization reaches its maximum at roughly uniform altitude throughout wavelength interval from 20 nm to 90 nm [11]. It allows this part of spectrum to be presumed effectively monochromatic when it comes to photoionization. The intensity of solar radiation in the discussed wavelength interval is significantly higher than at shorter wavelengths, while photons at longer wavelengths do not have a sufficient energy to ionize. The photoionization is thus governed mainly by the 20 to 90 nm interval.

There are many models that try to explain the formation and processes in the ionosphere. However, they are often quite complex with numerous parameters, which limits their usage on large sets of data. One simple model has been shown to agree reasonably well with profiles measured by radio occultation, even though it uses many

rather bold assumptions, that are not valid in the Martian ionosphere [1]. This so-called Chapman model conforms well to the part of the density profile close to the peak electron density, although it predicts only a single layer with a density maximum, which is inherently inaccurate due to the existence of additional local maxima at lower altitudes.

The Chapman model assumes that there is no plasma transport, the incident solar radiation is monochromatic, and the atmosphere has a uniform composition with the density decreasing exponentially with altitude. Furthermore, it is assumed that the absorption of the incoming solar radiation is proportional to the atmospheric density and to the radiation intensity. The plasma is eventually lost (transformed back to neutrals) by recombination. The recombination rate for species with a density of ionized particles n is αn^2, with recombination constant α is considered to be constant throughout the whole atmosphere [12].

When it comes to the altitudinal dependence of the photoionization, two main effects that oppose each other shape the final profile of the photoionization rate. The first is the concentration of neutral particles to be ionized. Higher concentrations of neutral particles result in higher ionization rates. However, the higher concentrations are found at lower altitudes deeper inside the atmosphere (see Figure 3). The ionization rate also grows with the solar radiation intensity. However, the solar radiation intensity diminishes with decreasing altitude. These two opposing effects combined thus result in an ionization rate maximum at a certain altitude (see Figure 4).
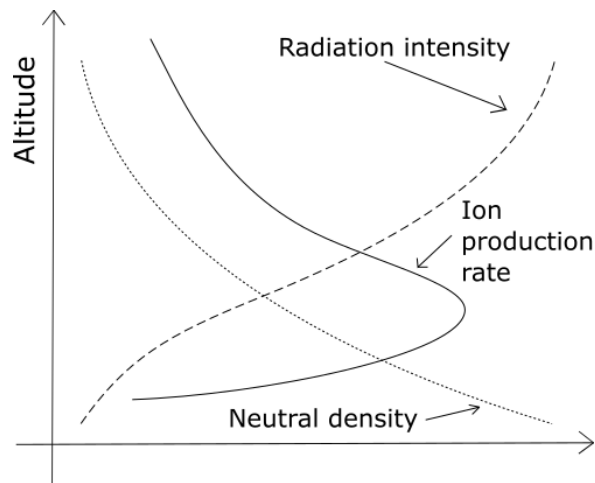

Figure 4 - Simplistic illustration of the formation of the Martian ionosphere, resulting in a single ionospheric layer.

According to the Chapman model, the altitudinal dependence of the electron density can be described as:

$$n(z) = n_m \exp\left\{\frac{1}{2}\left[1 - \frac{z - z_m}{H} - \exp\left(-\frac{z - z_m}{H}\right)\right]\right\} \qquad (1)$$

where n_m is the peak electron density, z_m is the altitude of peak electron density, and H is the neutral scale height. Peak electron density is a function of solar zenith angle (SZA):

$$n_m = \frac{n_0}{\sqrt{Ch}} \qquad (2)$$

where n_0 is peak electron density in the subsolar point and Ch is called Chapman grazing incidence function and it is dependent on SZA. The Chapman grazing incidence function represents the fact that the light traveling from the Sun to a location with higher SZA must travel through longer stretch of atmosphere before reaching the same altitude as at the subsolar point. Due to this longer path, the solar radiation is attenuated to the same degree at higher altitude and the altitude of the peak photoionization is offset higher. For smaller SZAs, corresponding to the dayside, this function can be approximated as $\sec(SZA)$ [12]. The altitude of peak electron density is then offset from the peak altitude at the subsolar point z_0 as:

$$z_m = z_o + H\ln(Ch) \qquad (3)$$

Some of the assumptions of the Chapman model can be thought as quite valid. For instance, the photoionization does not seem to depend significantly on the wavelength in the interval of 20 to 90 nm, making it effectively monochromatic. The ionospheric production is dominated by CO2, a single species. Based on usual conditions around the peak altitude, recombination happens on timescales smaller than diffusion, therefore neglecting the transport appears also rather reasonable [13]. This last assumption is, however, valid only on the dayside (SZA lower than 90°), while cross-terminator transport plays an important role at larger SZAs [14]. Additionally, since there is no EUV solar radiation on the nightside, the impact ionization by energetic particles precipitating to the ionosphere becomes essential, resulting in a patchy ionosphere controlled significantly by crustal magnetic fields [15].

1.4 Spectral analysis

One way to study the fluctuations of a measured signal in space/time is by calculating the Fourier transform (FT), since it breaks down the signal according to frequencies of its harmonic components. However, the measured signal is not a continuous function, but rather a sequence of measurements with a given sampling frequency. Considering the finite number of measurements and the discrete nature of the data, the Fourier transform can be modified to work with discrete data. One main difference is that the frequencies in the Discrete Fourier transform (DFT) domain are discrete and limited by the sampling frequency. The frequencies in the DFT domain are:

$$f_n = \frac{n}{N} f_s \tag{4}$$

where N is the number of measurements used for DFT, f_s is the sampling frequency, and n is a non-negative integer number up to $N/2$. Equation for calculating the nth coefficient becomes a sum, rather than an integral. There are various ways to compute these coefficients, but one of the most used is called Fast Fourier transform, which is usually implemented in readily available libraries.

Using modified Parseval relation for DFT Fourier coefficients can be transformed to represent the power associated with each frequency in a signal. Power spectral density (PSD) of a signal at frequency f_n can be then calculated as:

$$S_u(n) = \frac{2N}{f_s} |\tilde{u}(n)|^2 \tag{5}$$

where $\tilde{u}(n)$ is nth Fourier coefficient [16].

Using FT on a whole dataset is useful when dealing with stationary phenomena. However, when studying dependencies on parameters that change during data acquisition, a different approach is useful. Moving a window through the data to calculate DTF from small portions of measurement allows to analyse changes of PSD with time or other selected parameters. This technique is called Windowed Fourier transform (WFT).

1.5 Turbulent behaviour

Turbulent behaviour is a complex problem in fluid dynamics that may be applicable in the ionosphere as well. It has been demonstrated that the Kolmogorov's turbulence law can describe power spectra of magnetic variability in the Martian ionosphere [17].

Kolmogorov in his paper studies theoretical explanation for behaviour of fluid in a turbulent mode. Turbulent flow is composed of differently sized eddies, where the larger ones are more unstable. They then break up into smaller ones and so on until they eventually dissipate. These eddies are characterised by their length scales (dimensions) and their velocity scales. They carry kinetic energy which is passed down to smaller eddies upon their dissipation. If their velocity transformed by Fourier Transform is used to calculate kinetic energy, then the total kinetic energy of the system can be written as an integral of energies associated with different length scales. According to Kolmogorov, the energy associated with each length scale k is:

$$E(k) = C\, k^{\alpha} \qquad (6)$$

where C is a constant of a particular system [18]. The value of C depends on the energy of the system in question, but the value α is expected to be the same for all systems of turbulent flow. The expected value of α is -5/3, hence the name the Kolmogorov's 5/3 law.

1.6 Turbulent behaviour in electron density data

The Martian ionosphere is not uniform and it has structures of various electron densities of various scales. When a spacecraft moves through the ionosphere, it can be, in the first approximation, assumed to move fast enough to make the observed variations spatial rather than temporal. The observed structures are thus effectively nearly stationary when several consecutive measurements are considered. Moreover, if sufficiently low number of consecutive samples is picked, the speed of spacecraft is effectively constant in that window. Since FT of such a signal in the spatial-frequency domain differs from the time-frequency domain only by a multiplicative constant corresponding to the speed of the spacecraft, it is not necessary to convert it. Power spectrum of a signal represented by its FT is related to contributions of changes at

individual spatial frequencies to physical energy density [16]. If a PSD is calculated using equation (5), the obtained spectra can be fitted by equation (6) and the dependences of the fit parameters studied [19].

1.7 Solar radio flux F10.7

The solar radio flux F10.7 is an index representing solar radiation intensity. The index is the average spectral intensity of radiation in 100 MHz wide interval around 2800 MHz frequency (wavelength 10.7 cm) radiated by the whole solar disk for a period of one hour, centred on the time in question. The flux is measured in the solar flux unit (sfu), one solar flux unit is $1\,\text{sfu} = 10^{-22}\,\text{W}\,\text{m}^{-2}\,\text{Hz}^{-1}$. The power radiated at wavelengths in the range of tens of centimetres is sensitive to conditions in the upper chromosphere and the corona. Moreover, the Earth's atmosphere is almost transparent for the radiation at these wavelengths and respective ground measurements are therefore not distorted by the atmosphere [20]. Importantly, the solar radiation intensity at F10.7 wavelengths is well correlated with the solar radiation intensity at short wavelengths responsible for the ionospheric formation. The solar radio flux F10.7 index can be thus used as a proxy for the solar ionizing radiation.

The F10.7 index is historically measured at Earth and for use at Mars must be corrected. The Earth and Mars orbit at different orbits, therefore their distance from the Sun is different and must be accounted for. Considering that the intensity of radiation decreases with a square of the distance, the intensity at Mars can be easily calculated from the known Sun-Mars and Sun-Earth distances at the time of a measurement. The next correction is azimuthal. The Sun, Earth, and Mars are generally not aligned and the same spot on the Sun that irradiates the Earth thus does not irradiate Mars at the same time. Assuming the solar radiation from a given point does not change in time, the solar rotation can be used to provide the needed azimuthal correction. The same spot on the Sun that faced the Earth will face Mars at a later time. The solar flux measured at Earth is thus shifted in time proportionally to the Mars-Sun-Earth angle. This approach works reasonably well, as demonstrated by a direct comparison with MAVEN EUV data [21].

2. Aims of the Thesis

Martian ionosphere is a very complicated subject of study. Although some of its behaviour is well described by established models, there is still much variability not yet well understood. With data from recent orbiters, unprecedented detailed studies of this ionospheric system became feasible. Since still not much is known about all the factors that play role in shaping the ionosphere, this thesis tries to uncover what factors and how influence its formation. In this work, the variability of the Martian ionosphere is studied by analysing the deviations from expected simple behaviour as a function of other parameters which are unaccounted for, such as crustal magnetic field magnitude. The individual goals of the thesis can be summarized as:

1. Prepare an overview of former studies of the ionosphere formation and variability.

2. Familiarize oneself with the instrumentation of Mars Express and MAVEN orbiters and basic data processing.

3. Evaluate the influence of crustal magnetic fields and other relevant parameters.

4. Analyse deviations of peak electron densities from expected dependences.

5. Characterise electron density fluctuations.

3. Data

A data from two different instruments onboard two different spacecraft was used in this thesis: i) radar sounding data from the Mars Advanced Radar for Subsurface and Ionosphere Sounding (MARSIS) instrument onboard the Mars Express orbiter and ii) data from the Langmuir Probe and Waves (LPW) instrument onboard the MAVEN spacecraft. Both these instruments measure electron densities in the Martian ionosphere, and both are still operating to this day.

3.1 Mars Express

Mars Express is the first ESA mission to a planet other than the Earth. Launched in June 2003 from Baikonur Cosmodrome, it reached the red planet in December of the same year. The orbiter is a 3-axis stabilised and possesses a fixed high-gain antenna. The payload consists of several body-mounted instruments for remote and in situ measurements of planet interior, subsurface, surface, and atmosphere. Among many instruments it carries is the MARSIS instrument that provides a bulk of data used in this thesis.

Mars orbiter is placed on an elliptical orbit with a periapsis altitude of about 250 km and an apoapsis altitude of about 10,000 km. The quasi-polar orbit has an inclination of 86.35° and an orbital period of 6.75 h. The orbit was optimised to provide a wide surface coverage and communication with the Beagle 2 lander, as well as with other future landers [22].

3.2 MARSIS and ionosphere sounding

Radar sounding typically assumes that the ionosphere is horizontally stratified to make the measurement interpretation feasible. Moreover, since once the electron density in a region rises to a value, no lower electron densities can be measured beyond this region. The topside ionospheric sounding thus provides us with information about the ionosphere at altitudes between the spacecraft altitude and the altitude of peak electron density. The sounding works by sending a radar pulse of a certain frequency down through the ionosphere, while measuring the time until a reflection from the ionosphere returns to the spacecraft. A radio pulse with a frequency lower than the

plasma frequency cannot propagate through plasma. It is therefore reflected at a boundary where the plasma density reaches such a value that the plasma frequency becomes equal to the frequency of the pulse. The plasma frequency in Hz is given by $f_p = 8980 \sqrt{n_e}$, where n_e is electron density in cm^{-3} [23]. The frequency of the reflected pulse is thus directly related to the electron density in the region of the reflection. Moreover, the measured time delay is related to the distance between the sounder and the reflection region. As the sounder performs many measurements with incrementing sounding frequency in a quick succession, it possible to eventually evaluate the entire vertical electron density profile between the spacecraft location and the peak altitude (see Figure 5).
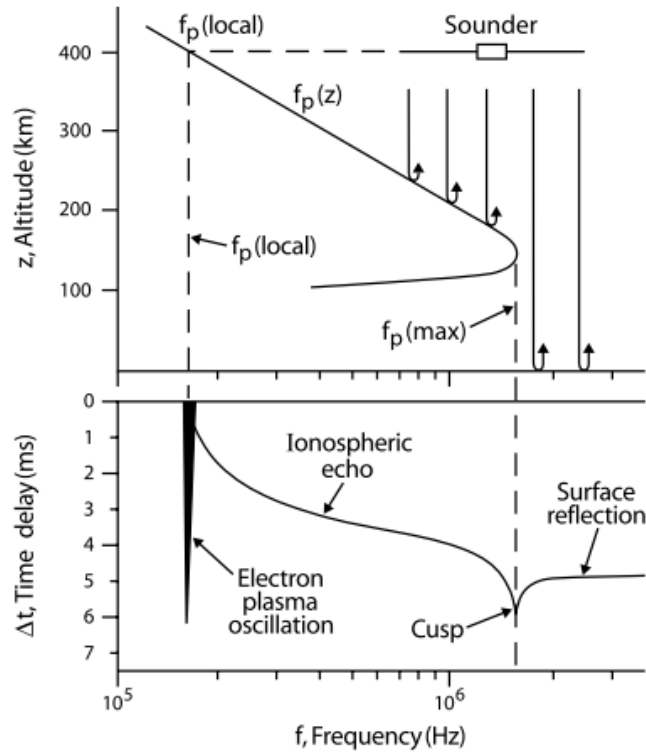

Figure 5 - (top) Principle behind the radar sounding of a horizontally stratified ionosphere. (bottom) Resulting ionogram. The dashed lines show a relationship to the ionospheric features at the top panel. (Adopted from [24].)

An ionogram is a 2D plot of detected signal intensity as a function of the signal frequency and time delay. Ionograms measured by MARSIS typically contain not only the envisaged vertical ionospheric reflections, but also specific additional signals (see Figure 5). Usually, there are harmonic signals at low frequencies that extend through principally the entire range of time delays. These signals are due to local electron plasma oscillations, which are excited in the plasma during the pulse transmission. Following that on the frequency scale, there is an ionospheric echo, which follows the

electron density in the ionosphere, until it reaches its peak electron density, forming a cusp. A cusp is formed at a frequency where the ionospheric reflection meets the reflection from the surface of the planet. The higher the frequency of the radar pulse, the weaker is the influence of the passing through ionosphere on the group velocity. Pulses with a frequency higher than the peak frequency of the ionospheric reflection thus return sooner than some of the pulses with frequencies near the cusp. Such reflections, however, are not reflections from the ionosphere, but rather from the surface of the planet, and they are therefore uninteresting for most ionospheric studies [23].
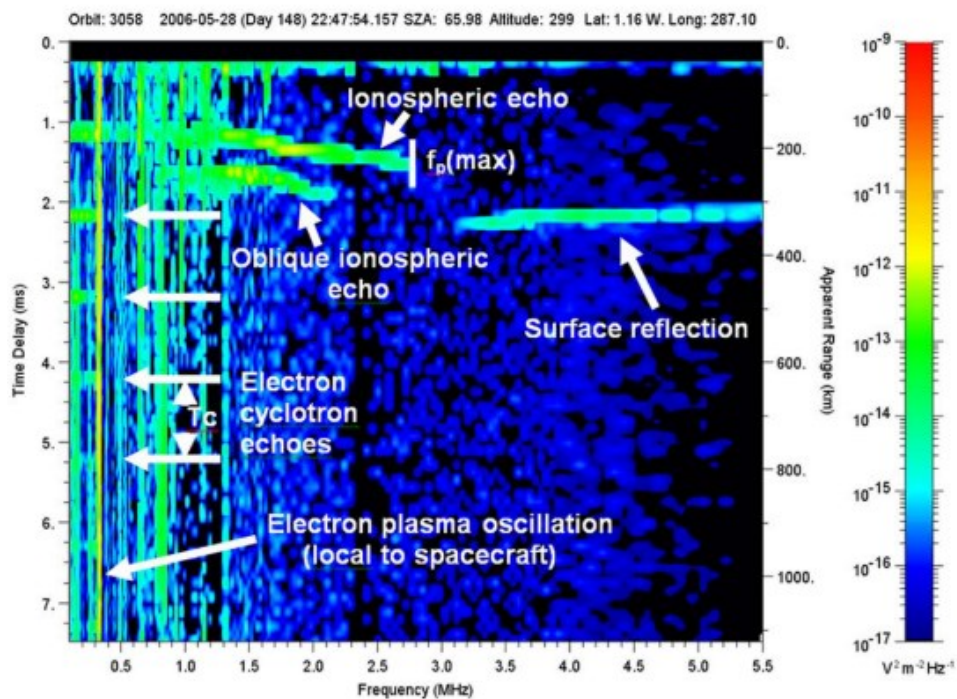

Figure 6 - An example of measured ionogram, showing all discussed structures.
(Adopted from [25].)

In actual ionograms, there are a few more structures (see Figure 6). There can be an oblique echo, which looks similar to the primary ionospheric echo, but at larger time delays. Since the corresponding ionospheric feature cannot be situated at altitudes lower than the ordinarily sounded ionosphere, a logical conclusion is that this signal is a reflection coming from another direction, being reflected off of a region with higher electron density not below the spacecraft. This information is typically unusable for direct ionospheric studies, as it is not clear from which direction the reflection returned. Another feature sometimes present in ionograms are electron cyclotron echoes. They manifest themselves as echoes equally spaced in time along the left edge

of an ionogram. The period of their repetition almost exactly matches the local cyclotron frequency [23]. The mechanism of the formation of cyclotron echoes is believed to be due to a strong electric field near the antenna accelerating electrons at the time of the transmission, which subsequently periodically move to the vicinity of the receiver antenna due to the present ambient magnetic field

MARSIS in the Active Ionospheric Sounding (AIS) mode measures up to the maximal altitude of about 1200 km (the instrument is not turned on at the times when the spacecraft is at higher altitudes). A frequency sweep starts at 100 kHz and finishes at 5.5 MHz. The total number of frequencies radiated/received in the measured frequency interval is 160. The sounding frequencies are quasi-logarithmically spaced, with $\Delta f / f \approx 2$ %. The sweep is repeated every 7.54 s [25].

3.3 Ionogram inversion

In the first approximation, it can be assumed that the radar pulse travels at the speed of light in a vacuum. The altitude of the signal reflection calculated in this way is called apparent height. The apparent height is not entirely correct. The farther and deeper inside the ionosphere the pulse penetrates, the more is the apparent height off due to the difference between the signal group velocity and the speed of light in a vacuum. The apparent height is usually used as the secondary axis to the time delay axis.

To calculate the proper altitude of the signal reflection, so called corrected altitude, plasma parameters along the entire propagation path need to be considered. The time of the signal propagation between the spacecraft and the altitude with the plasma frequency equal to the pulse frequency and back is given by:

$$\Delta t(f) = \frac{2}{c} \int_{z(f)}^{z_{sp}} \frac{dz}{\sqrt{1 - \left(\frac{f_p(z)}{f}\right)^2}} \tag{7}$$

where $z(f)$ is the altitude of the reflection, z_{sp} is the altitude of the spacecraft, f is the frequency of the pulse and $f_p(z)$ is the dependence of plasma frequency on the altitude. To calculate the altitude of reflection, equation (7) has to be inverted. The inversion is given by:

$$z(f) = \frac{2}{\pi} \int_{\alpha_0}^{\pi/2} \frac{c}{2} \Delta t(f \sin \alpha) d\alpha \qquad (8)$$

where $\sin \alpha = f_p(z)/f$ and $\sin \alpha_0 = f_p(z_{sp})/f_p(\max)$ [24]. It is obvious that to calculate the reflection altitude, the plasma frequency at all higher altitudes must be known. Previous measurements from the same sweep are used for this part of the dependence, and the procedure is iteratively repeated to get the entire altitude profile. However, due to technical reasons, the power radiated by MARSIS at low frequencies is typically too low for the reflected signals to be detectable. The electron densities at altitudes just below the spacecraft thus cannot be measured by the ionospheric radar sounding. The electron densities in this altitudinal region, spanning between the spacecraft (where the electron density can be determined from local plasma oscillations) and the highest altitude where the electron density is high enough to be measured by the ionospheric radar sounding, have to be obtained by interpolation, for example assuming the dependence to be exponential (see Figure 7).
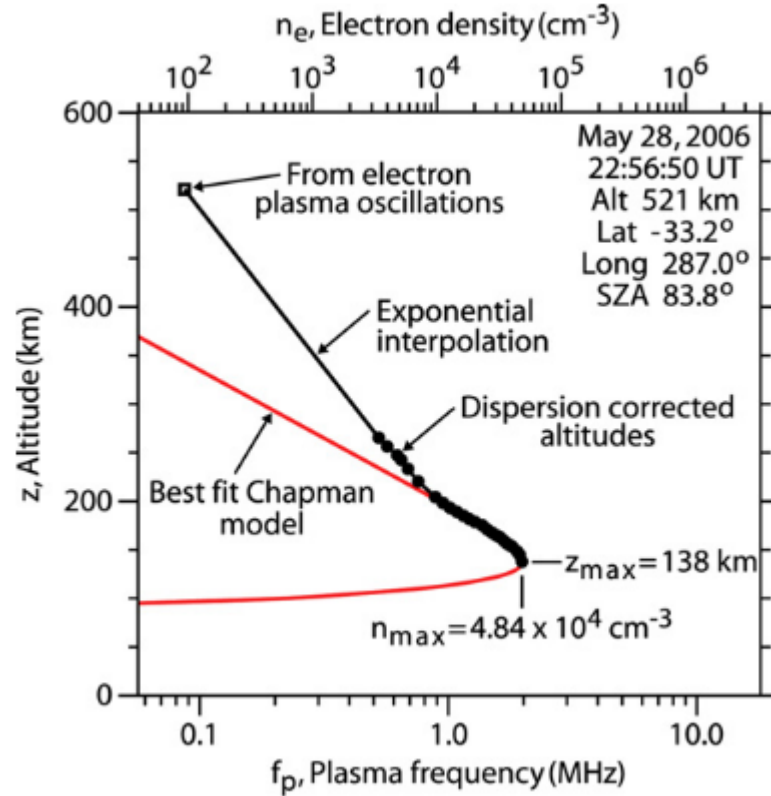

Figure 7 - Example of an electron density profile measured by the MARSIS instrument. The red curve corresponds to the best fit Chapman profile. Exponential interpolation is used in the altitudinal region between the spacecraft and the first radar sounding measurement. (Adopted from [24].)

16

3.4   MAVEN

Mars Atmosphere and Volatile Evolution (MAVEN) is a NASA spacecraft built to study the Martian upper atmosphere and ionosphere. Launched in November 2013, it inserted into orbit around Mars in September 2014. As of now, its mission is still active, collecting valuable data about the Martian ionosphere. The MAVEN payload is mainly geared toward in situ measurements and so is its orbit. The orbit is elliptic with the apoapsis altitude of about 6200 km and the periapsis altitude as low as about 150 km ("deep dip"). Thanks to its low periapsis altitude, MAVEN can measure parameters of plasma close to a region of peak electron density during the deep dip orbital phase. The inclination of its orbit is 75° and the orbital period is 4.5 hours. It is equipped by several instruments to study the atmosphere and ionosphere, data used in this thesis were obtained by the Langmuir Probe and Waves instrument [26].

3.5   Langmuir Probe and Waves

LPW is an instrument used for in situ electron density and temperature measurements. The electron density measurements are carried out by measuring the whole I-V characteristic. The measurement itself consists of measuring a current into voltage biased probe. This is performed in a short pseudo-logarithmic sweep, designed to optimise the accuracy of temperature measurements [27].

The spacecraft has two probes that can be used in two modes. First mode uses each probe separately to measure electron concentration and temperature. However both probes are used for Langmuir Probe (LP) sweep in order to avoid measuring plasma parameters in wake of the spacecraft. Second mode is the waves mode, which uses both probes essentially as voltmeters to measure fluctuations in electric field [28].

3.6   Data used in this thesis

Electron density data used in this thesis originate from the two spacecraft introduced in preceding subchapters, Mars Express and MAVEN.

As discussed in sub-chapter 3.3, the output of the MARSIS measurement is an ionogram that must be inverted to get the profile. A state-of-the-art inversion method

described in [29] with subsequent improvements suggested in [30, 31] is routinely applied to digitized MARSIS ionospheric traces at the University of Iowa, Iowa City, IA, USA, and the resulting electron density profiles are used in the thesis.

MAVEN data needs no such inversion and the publicly available data already contains electron densities [27].

Mars Express data from July 2005 until November 2015 (orbits from 1909 to 14916) are used in the analysis, in total 285,988 electron density profiles. The MAVEN data used span from November 2014 to January 2017, corresponding to 1,012,433 electron density measurements.

The supplemental magnetic field data used to characterize the magnitude and orientation of crustal magnetic fields are based on a widely used model developed using data provided by Mars Global Surveyor [32]. The model vector magnetic fields are evaluated at an altitude of 400 km. This is close to the altitude where the data used for the model construction were acquired, and it is well suitable for characterizing the crustal magnetic field configuration above the ionospheric peak.

4. Results

4.1 Average electron density dependences

We study overall dependences of measured electron densities using data from both the Mars Express spacecraft and the MAVEN spacecraft. All measurements are organized according to the altitude of measurement and the SZA of the spacecraft at the time of measurement. The bins in altitude start at 100 km because no MAVEN measurements and very few MARSIS measurements are taken below that point. Moreover, since the electron peak density is expected around 130 km, many of those measurements below 100 km are likely erroneous, stemming from artifacts in MARSIS ionospheric traces. Similarly, rare MARSIS electron density profiles with peak altitudes above 200 km are discarded as incorrect as well. Finally, measurements at altitudes above 320 km are also disregarded, since these are out of our primary focus, are potentially affected by the presence of the ionopause, and the corresponding densities are principally always below the MARSIS sounding threshold and they are thus based purely on the interpolation. The whole domain of SZA is used, ranging from 0° up to 180°. The bin widths are 10 km and 10°, respectively.

With data divided this way, average electron density is calculated for all bins. Moreover, the same approach is used to calculate average densities also for two specific subsets, the first being only measurements at locations with low model crustal magnetic field magnitude at 400 km (B < 5 nT) and the second at locations with high crustal magnetic field magnitude (B > 20 nT). Other variants of the analysis, trying to reflect different crustal magnetic field inclinations, do not reveal any significant difference between the low/high situations and they are not considered further (not shown).

Figure 8 shows the obtained results in a form of colour coded average electron densities measured by Mars Express as a function of the altitude of measurement and SZA. There are three panels. The first panel contains data regardless of the magnitude of the crustal magnetic field, the second panel shows average electron densities calculated only from measurements taken at locations with low crustal magnetic field magnitude, and the third panel depicts average electron densities calculated only from measurements at locations with high crustal magnetic field magnitude. There are some

differences between the three panels. The high crustal magnetic field magnitude case has on average higher densities than the other two. Moreover, in the region of lower SZAs and altitudes between 150 and 200 km, the start of the rapid increase in electron density is lower for weak crustal magnetic fields and higher for stronger crustal magnetic fields than in the average situation.

Figure 8 – The average electron density dependence on the SZA and the altitude, for three different cases of the crustal magnetic field magnitude. Measured by Mars Express.
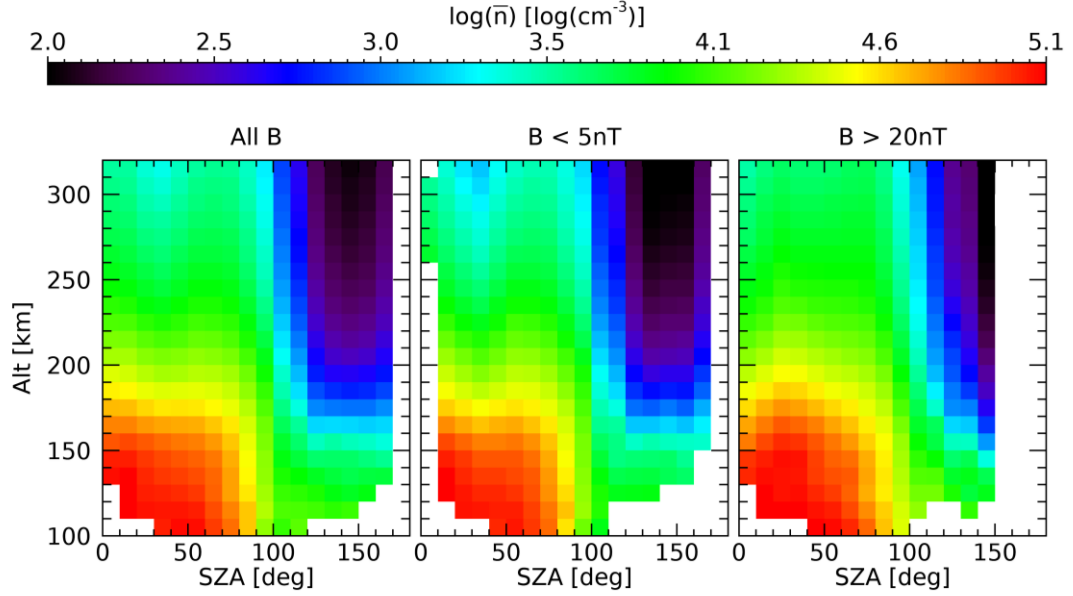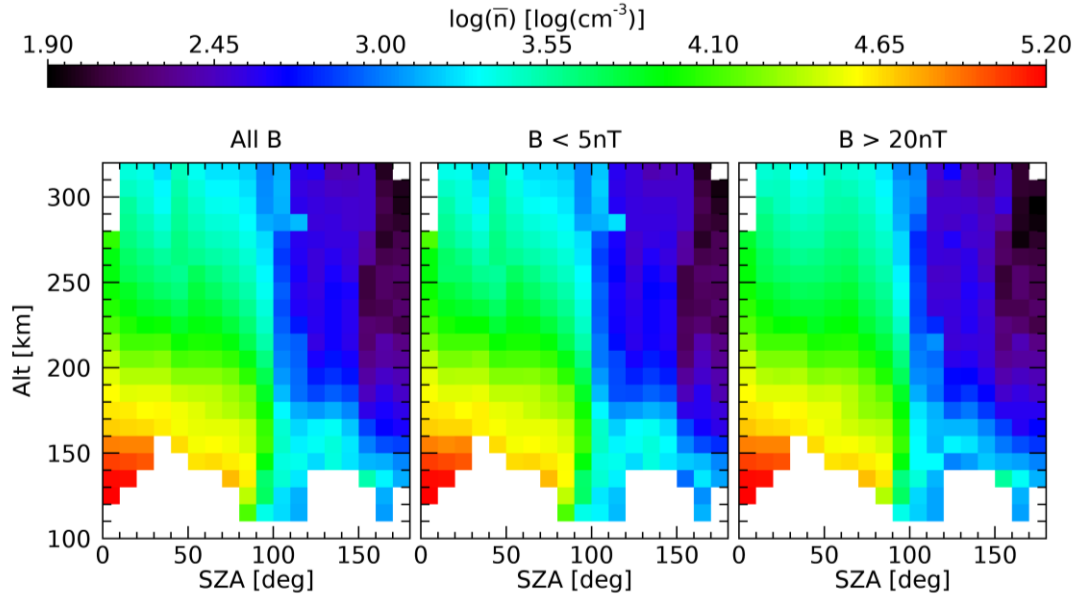

Figure 9 – The average electron density dependence on the SZA and the altitude, for three different cases of the crustal magnetic field magnitude. Measured by MAVEN.

The data from the MAVEN spacecraft is processed in the very same way as the data from Mars Express. This time none of the data is discarded since there is no risk of ionospheric trace artifacts and/or oblique reflections with the direct in-situ Langmuir probe measurements.

Average electron densities measured by MAVEN presented in Figure 9 behave similarly to the electron densities measured by Mars Express. The same three cases are plotted, i.e., all crustal magnetic field magnitudes, low crustal magnetic field magnitudes, and high crustal magnetic field magnitudes, respectively. The figures show the same effect of the magnetic field, with overall higher electron densities being observed at locations with stronger crustal magnetic fields, in particular at higher altitudes. One technical difference is that the MAVEN data does not extend down to 100 km, for some SZAs only down to 150 km. This is because the usual periapsis of MAVEN is as high as around 150 km, and the spacecraft only occasionally dips lower.

4.2   Deviations from the Chapman model

For this analysis, only data from Mars Express is used. For each orbit, all peak electron densities were fitted by equation (2), where the Chapman grazing incidence function was approximated $Ch = 1/\cos(SZA)$, which is a very accurate approximation for not too large SZAs. In this regard, only the data measured at SZAs lower than 75° are used for the analysis. Additionally, a sufficient number of data points spanning a considerable range of SZAs is needed to capture the SZA dependence properly. Therefore, only orbits with at least 20 electron density profiles measured at SZAs below 75° and with the difference between the lowest and the highest SZA at least 30° are used. The last condition is to ensure that sufficiently large domain of the fitted function is covered, to avoid fitting bunched up measurements.

All orbits that meet these conditions are fitted and the average root mean square difference from the fit is calculated for each orbit. Based on a visual inspection, an upper threshold for the difference is set at 10^4 cm^{-3}. Altogether, there are 218 orbits that meet all the aforementioned conditions. An example of the SZA dependence of peak electron densities measured during one such an orbit with a Chapman fit overplotted is shown in Figure 10.
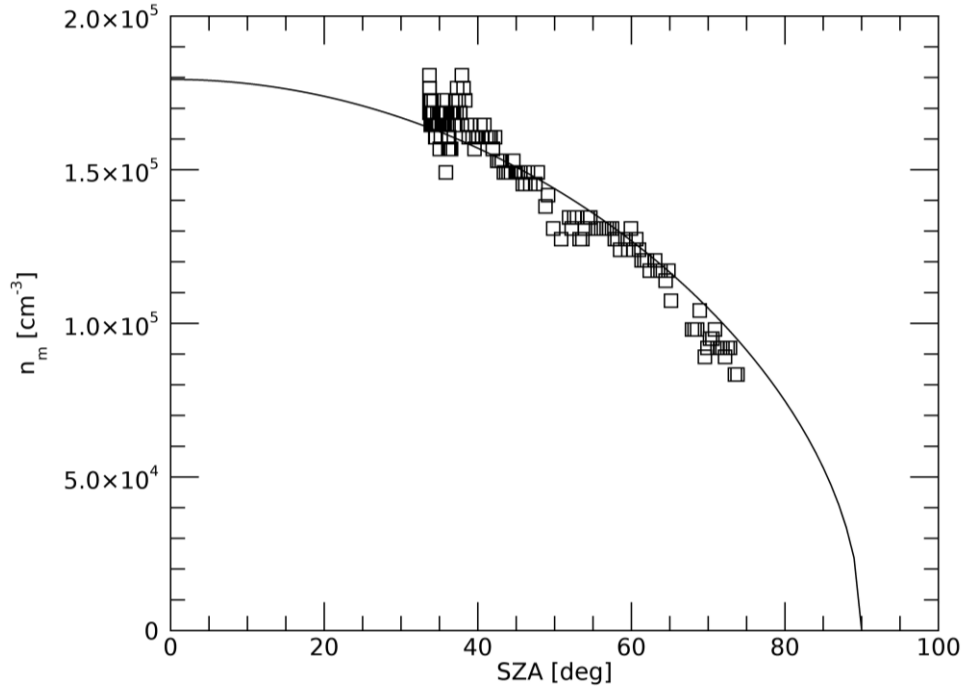
Figure 10 - An example of the SZA dependence of peak electron densities measured during a single orbit that meets the conditions (see text). The solid curve is the SZA dependence corresponding to the Chapman model.

The deviations of measured peak electron densities from the Chapman fit of the SZA dependence are calculated, and they are studied further to look for the variations of peak electron density as a function of other parameters. Two types of deviations are calculated: i) differences between the measured and fitted values, denoted $\Delta n = n_m - n_{fit}$ and ii) ratios between the measured and fitted values, denoted $\delta n = n_m/n_{fit}$. Both deviation types usually show similar behaviour (not shown), and therefore only the results obtained for the differences between the measured and fitted values are shown hereinafter.

The analysed dependences of the deviations from the Chapman-predicted SZA dependence on other parameters generally exhibit a significant scatter. In addition to individual data points, median values are therefore depicted in the figures. The horizontal red lines mark the median value in each interval they span, the interval widths are based on the units and extents of analysed parameters.
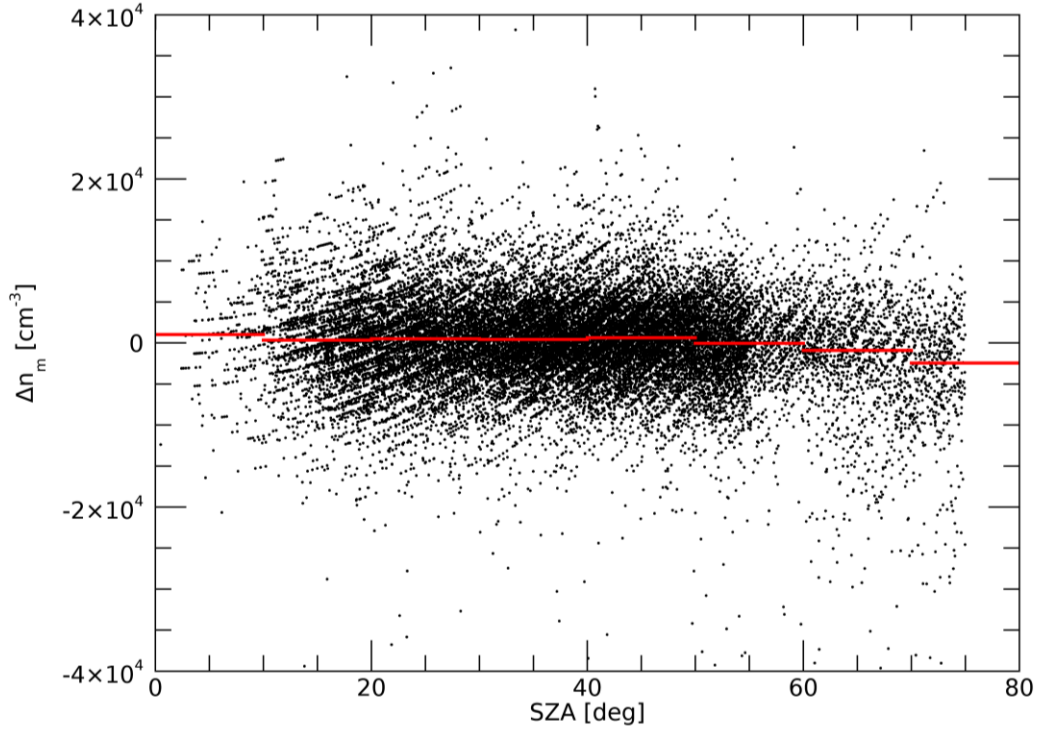
Figure 11 – The dependence of peak electron density subtractive deviation on the SZA. The red lines show median values in individual 10° wide SZA intervals.
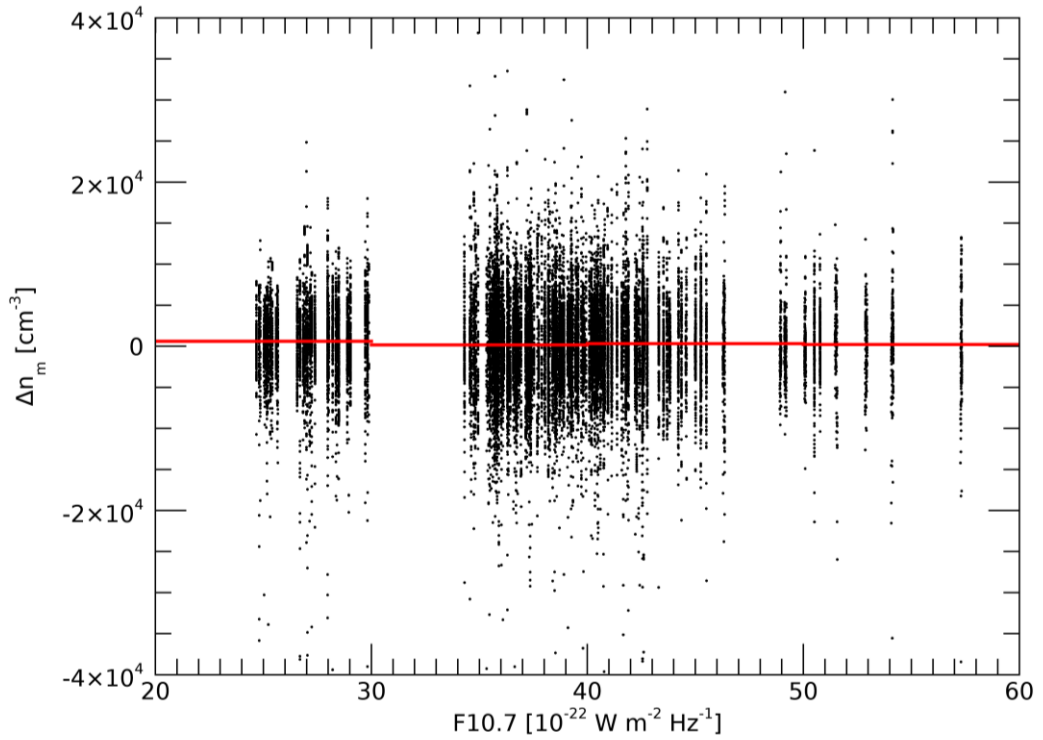

Figure 12 – The dependence of peak electron density subtractive deviation on the F10.7 solar radio flux. The red lines show median values in individual 10^{-21}W m^{-2} Hz^{-1} wide intervals.

The dependence of peak electron density subtractive deviations on SZA is plotted in Figure 11. The data points have a large scatter around the median values represented by the red lines, each spanning an interval of 10°. There are some outliers, but the majority of data points fall within the interval from -2.10^{-4} to 2.10^4 cm^{-3}. Furthermore, there is a noticeable change in the number of measurements around the SZA of 55°. There might be a very slight trend for the median deviation value to decrease beyond this SZA.

Upon closer inspection the data points seem to group in rising curves. Almost the same behaviour can be seen in the division deviation, differing mainly in the outlier measurements. These are related to the discrete sounding frequencies of the MARSIS instrument, which typically result in peak electron densities measured in adjacent SZAs to be the same, while the Chapman-based predicted peak electron densities decrease smoothly with increasing SZA.

The solar radio flux F10.7 is tested as a possible parameter for the peak electron density subtractive deviation in Figure 12. It differs quite significantly from the dependence on SZA in the way that there are several empty or almost empty intervals in the F10.7 domain. The median values show virtually no dependence on F10.7. The apparent grouping of data points into vertical lines is a result of the MARSIS instrument data coverage. Essentially, each vertical group of points corresponds to the data acquired during the periapsis pass of the same orbit (recall that the instrument did not operate at high spacecraft altitudes).

The last dependence of the subtractive deviation is shown in Figure 13. The parameter here is the model crustal magnetic field magnitude at an altitude of 400 km. No obvious trend can be seen, the individual data points are roughly symmetrically distributed around the median lines. On a closer look, while the median lines are very close to zero deviation for lower crustal magnetic field magnitudes, they tend to somewhat deviate toward positive values for stronger crustal magnetic fields. However, the number of data points at high crustal magnetic field magnitudes is quite limited and there are thus significant fluctuations and uncertainties present. Note that the crustal magnetic field magnitude axis is logarithmic in order to conveniently accommodate the large range of magnetic field magnitudes present. Much the same as

before, the dependence of division deviations is very similar to the one shown in Figure 13.
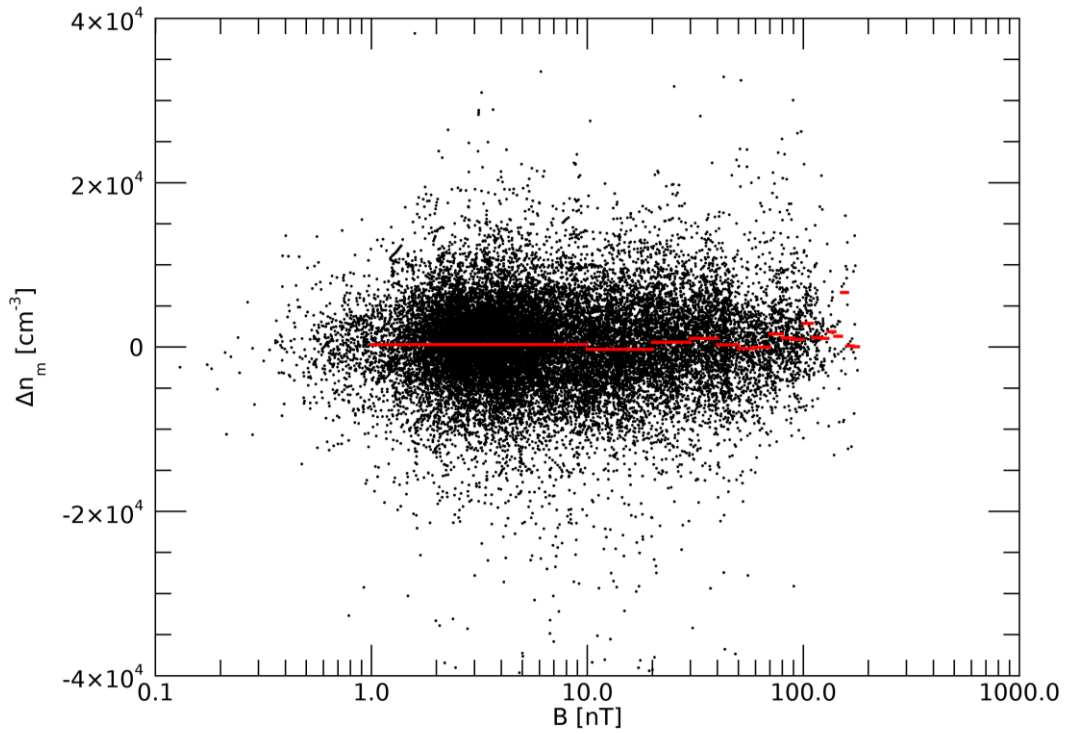

Figure 13 – The dependence of peak electron density subtractive deviation on the magnitude of crustal magnetic fields. The red lines show median values in individual 10 nT wide intervals.

The peak electron density in the subsolar point is a fit parameter for the whole orbit. A relationship between the peak electron density in the subsolar point and F10.7 solar radio flux is shown in Figure 14. In this figure, only orbits that had at least two-thirds of measured electron density profiles in the northern or in the southern hemisphere are considered. The idea is to check for possible differences between the hemispheres, keeping in mind that significant crustal magnetic fields are located primarily in the southern hemisphere. Unfortunately, the data coverage of the northern/southern hemisphere and low/high solar radio fluxes does not allow for such a direct comparison. Specifically, while the data for low solar radio flux (less than about $30 \cdot 10^{-22}$ W m^{-2} Hz^{-1}) is taken primarily in the northern hemisphere, the data measured at the times of high solar radio fluxes is taken primarily in the southern hemisphere. Nevertheless, the curve overplotted in the figure is a fit proportional to the square root of F10.7, which matches the data measured in both hemispheres well enough.
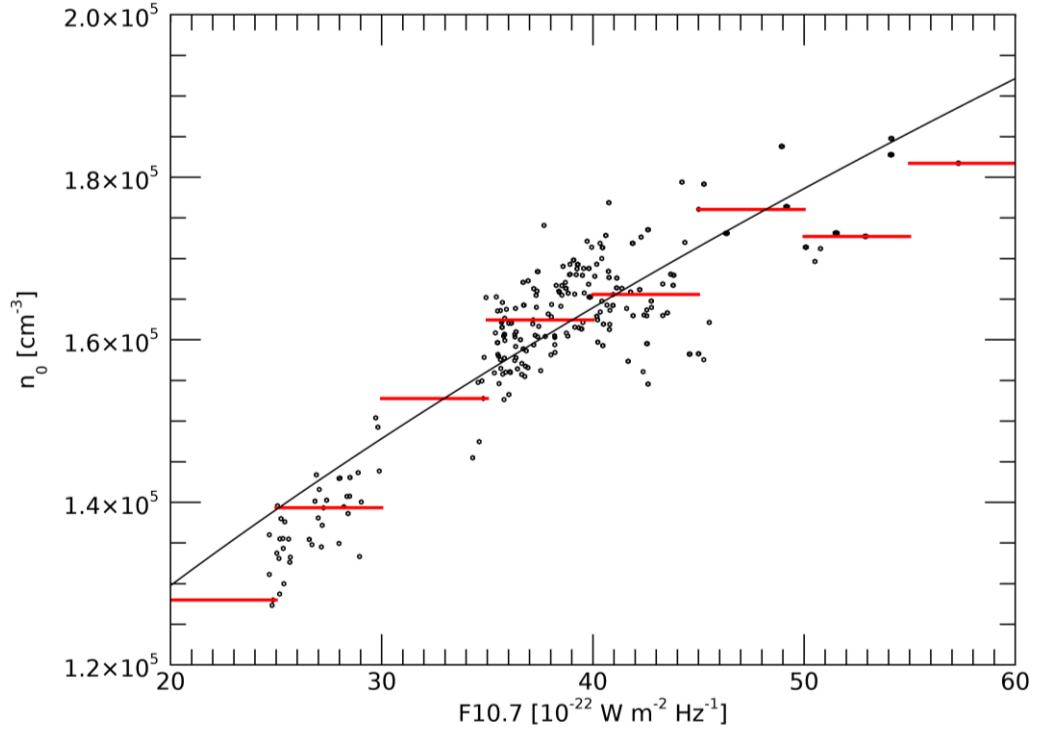
Figure 14 – The dependence of peak electron density in the subsolar point on the F10.7 solar radio flux. The red horizontal lines show median values in individual $10^{-21} \text{W m}^{-2} \text{ Hz}^{-1}$ wide intervals. The curve corresponds to the best fit proportional to the square root of F10.7.

4.3 Spectra of electron density fluctuations

In this section data from Mars Express was used. The MARSIS measurements provide us with an electron density profile for each sweep (a given time). Considering the inversion routine and the related intrinsic smoothing of electron density profiles, it is not desirable to study short-scale variations of electron densities using single profile data. However, several consecutively measured electron density profiles can be used to achieve the goal. In order to analyse the variations of electron densities by the means of standardized routines for time series analysis, a specific electron density (e.g., at a particular altitude) must be thus chosen out of the entire electron density profile. Two different choices of this electron density are used. First, peak electron density in a given profile regardless of the altitude is used. Second, electron density at a fixed altitude (or rather a set of fixed altitudes) is used, which allows us to study the altitudinal dependence of the fluctuations.

4.3.1 Peak electron density fluctuations

Only electron density profiles with peak altitudes between 100 km and 200 km are considered, similarly to the subchapter 4.1. In order to achieve a consistent frequency domain between individual FFTs, the number of samples for each FFT must be the same. Only orbits that have enough samples for at least a single FFT are thus considered. The length of FFT is set to 64 points, which is a reasonable compromise between the requirement of a sufficient number of points in a single spectrum and the requirement of not too many subsequent electron density profiles needed for the calculation. Additionally, due to the properties of DFT, all the 64 samples need to be equidistant in time. This is normally the case, as two consecutive sweeps are separated by exactly 7.54 s. Should there be a missing sweep in the data, the respective time series is discarded from the analysis.

After extracting the appropriate peak electron densities from profiles, a FFT of all suitable time series is calculated. The resulting frequency spectra are then fitted as:

$$PSD = C \cdot f^{\alpha} \tag{9}$$

where C is a power factor and f is a frequency, essentially corresponding to equation (6). The peak electron density is usually on the order of 10^5 cm^{-3} and it does not follow any clear overall trend distinguishable in all orbits. However, typically, the peak electron density variation is monotonous, either rising or falling, depending on the direction of a particular orbit. There may be flat (nearly constant peak electron density) regions in peak electron densities in substantial portion of orbits. An example of peak electron densities measured during a single orbit (orbit number 2023) is shown in Figure 15. The plotted measurement time is expressed in seconds from the first measurement during the orbit. It can be seen that the peak electron density starts at high value, remains nearly constant for about 100 measurements (about 750 s), and then gradually decreases, suggesting that the start of the measurement was around the subsolar point.

One of the frequency spectra calculated for orbit 2023 is shown by the solid line in Figure 16. The dashed line is the fit of this frequency spectrum by the dependence (9). For this particular case, the value of the coefficient alpha is equal to about -0.839, which is significantly lower than expected. However, it can be seen that although the spectrum fluctuates significantly, its overall shape can be reasonably well fitted by
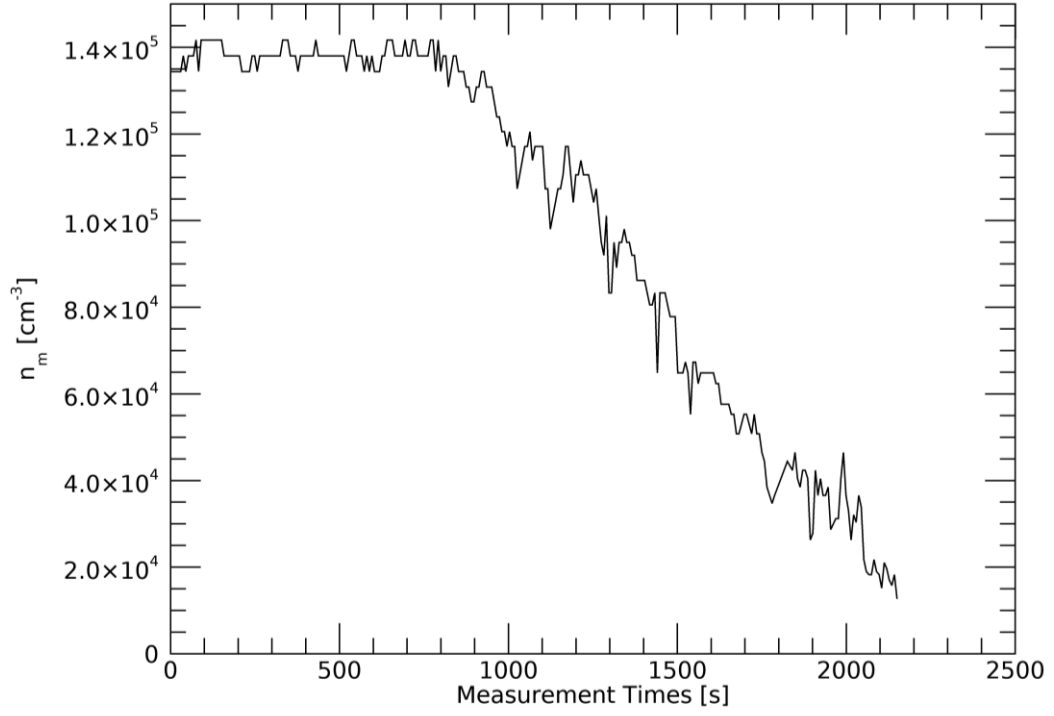
Figure 15 - An example of typical peak electron density measurements during a single orbit (orbit number 2023).
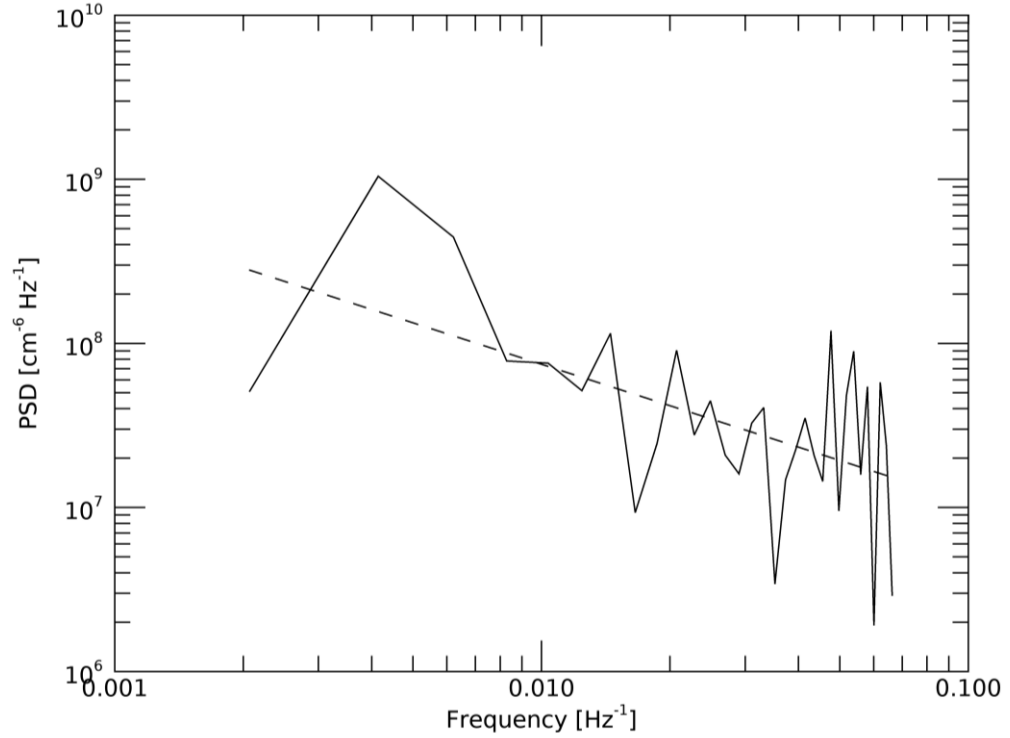
Figure 16 - An example of a frequency spectrum calculated for one of the time series from orbit 2023 is shown by the solid line. The dashed line corresponds to the power law fit given by equation (9).

the assumed power law dependence (a line in log-log scale). The output of the fitting are two parameters α and C. The first one represents the slope of the spectrum in the log-log plot and the second is a power factor with unit $cm^{-6} \, Hz^{-1}$. In order to allow an

analysis of the relative fluctuation power, it is desirable to normalize the power by the median electron density *nm* calculated over a given time series. We thus introduce a new parameter for each spectrum, defined as $C_n = C/n_m^2$, with units Hz^{-1}.

Frequency spectra which cannot be successfully fitted by the assumed power law dependence are discarded from further analysis. Uncertainties of respective fit parameters are used as a criterion. All spectra with an uncertainty of α higher than 0.3 or an uncertainty of C higher than a factor of 3 are discarded and they are not considered any further. Altogether, this leaves us with as many as 57 140 successful spectral fits for the analysis.

The resulting distribution of parameters α is shown in Figure 17. There is a peak around the value -1.7. The number of spectra with lower values of alpha falls very quickly. However, this is not the case for number of spectra with higher values of alpha, where the decrease is quite gradual, ranging all the way up to values of alpha close to 0. The red vertical line marks the median value of the entire distribution, which is about -1.4.
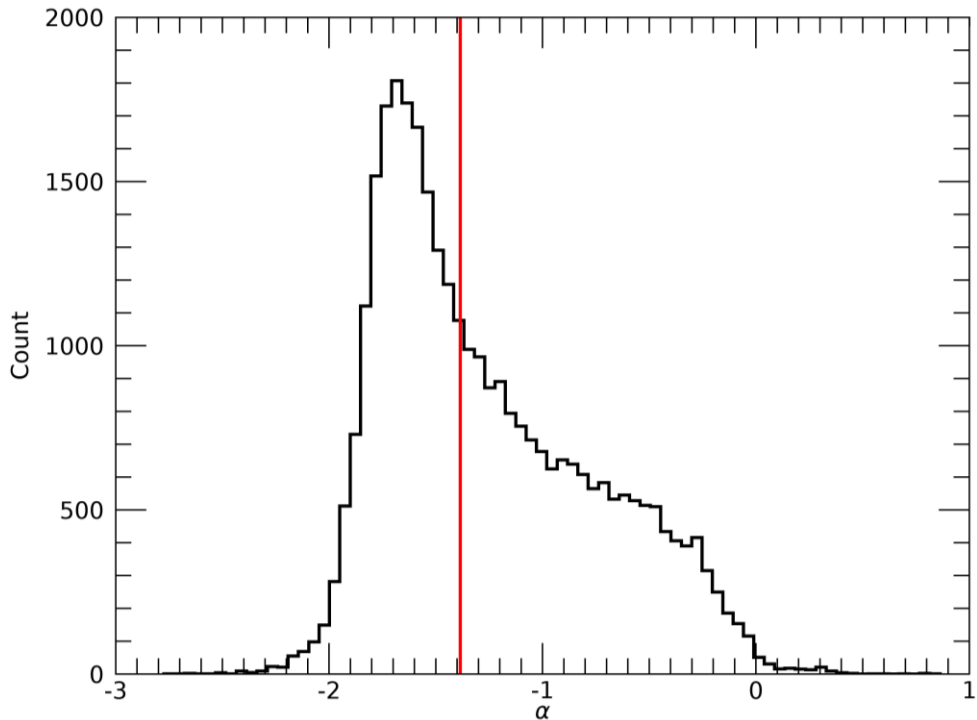

Figure 17 - A histogram of parameter α for all successful fits of frequency spectra. The red line marks the median value.
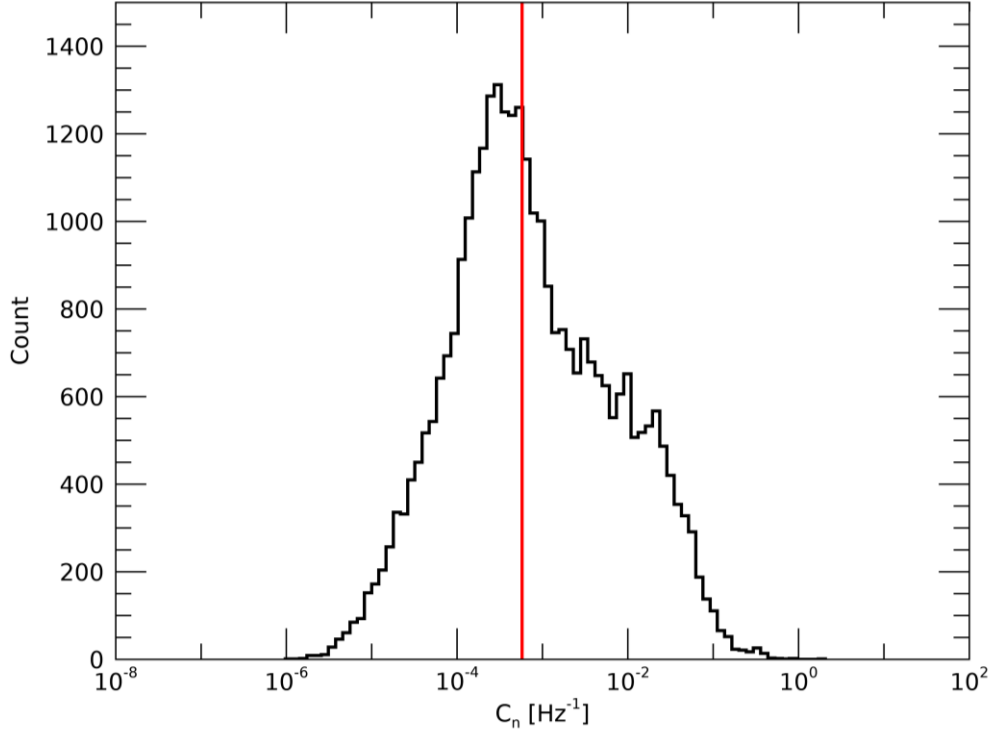
Figure 18 - A histogram of parameter C_n for all successful fits of frequency spectra. The red line marks the median value.

The histogram of the parameter C_n is shown in Figure 18. The red vertical line again marks the median value of the entire distribution. Although the distribution has quite a long tail at larger values, it is considerably more symmetric than the distribution of the parameter α. We note that the minor local maxima identifiable in the right-hand part of the distribution are likely only a statistical fluctuation not having and not of interest for the present study.

A natural parameter to investigate as possibly controlling the level and character of the peak electron density fluctuations is SZA, since the related grazing incidence function controls the amount of solar ionizing radiation and thus also the peak electron densities. The values of α as a function of SZA are shown in Figure 19. Each dot represents a single fit of the frequency spectrum and the red lines represent median values in individual 10° wide SZA intervals. We note that the SZA is clearly not constant along the 64-sample interval needed for the spectrum calculation. A median SZA value calculated over the used 64 consecutive electron density profile measurements is thus used for the purpose of this analysis. Most of the analysed spectra are obtained at SZAs between about 40 and 90 degrees, with only few spectra acquired at lower/larger SZAs.
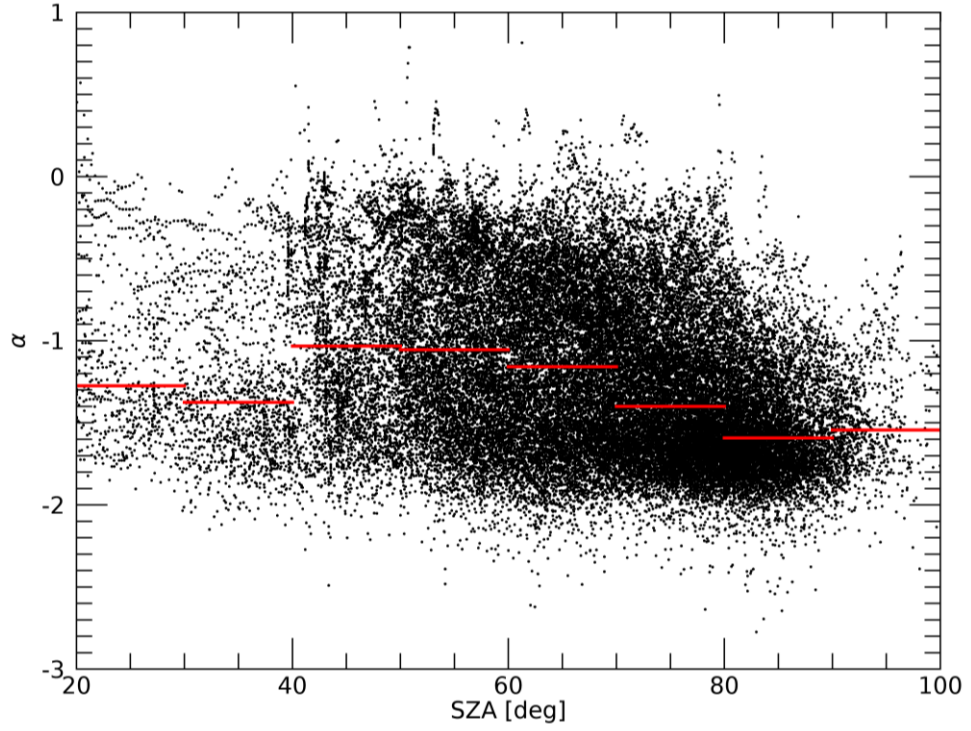
Figure 19 - The values of spectral fit parameters α as a function of SZA. The red lines represent median values in individual 10° wide intervals.

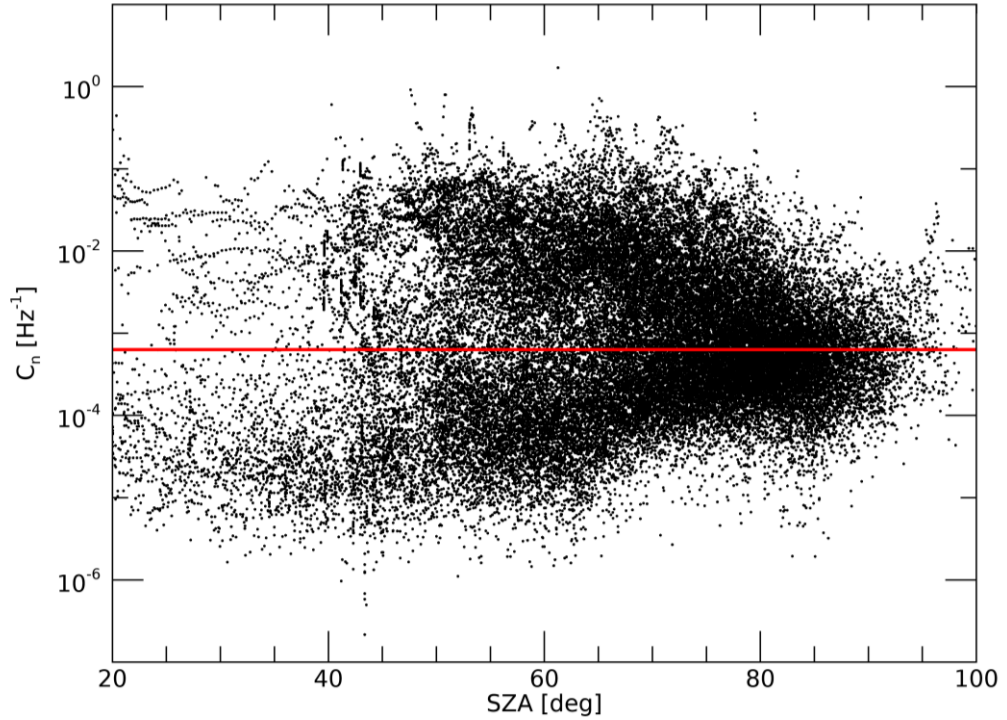**Figure 20 - The values of spectral fit parameters C_n as a function of SZA. The red line represents a median value of the entire data set.**

It can be seen that the majority of α values fall within the interval between -2 and 0. However, there is a clear trend for the upper limit on α to decrease with increasing SZA. On a closer look, there seem to be two quite distinct groups of data points. First,

there is a group of data points with lower values of α and only a weak dependence on SZA. Second, there is a group of data points with higher values of α, which systematically decrease with increasing SZA. A detailed inspection of the data reveals that the peak electron density time series used for the calculation of these spectra typically exhibit a sudden short-lasting drop of peak electron density (a single ionogram). It is questionable whether these specific measurements correspond to the real situation or if they rather indicate some technical issue with the radar sounding. This issue will be discussed more in detail in section 5.

The dependence of the C_n parameter on SZA is shown in Figure 20. Each dot again represents a single successful spectral fit, while the red line shows the median value calculated across the whole set. Note that, in this figure, a single median value is shown, as the two regions of the data points are now too distinct and exhibit strikingly different dependences. The bottom group of data points with C_n values of roughly 10^{-4} Hz^{-1} corresponds to the bottom group of data points in Figure 19, while the upper group of data points with C_n values of approximately 10^{-2} Hz^{-1} corresponds to the upper group of data points in Figure 19. While the values of α systematically increase with SZA for the lower group, they decrease with SZA for the upper group. The two groups of data points ultimately meet at large SZAs close to the median Cn value of about 5.10^{-4}. We note that this behaviour is in agreement with the aforementioned explanation based on the sudden short-lasting drops in peak electron densities – such a drop necessarily increases power spectral density over a wide range of frequencies, shifting the parameter α closer to 0.

Apart from SZA, the intensity of incoming solar ionizing radiation is considered as a possible controlling factor of power spectral densities and spectral shapes. Since direct measurements of the solar ionizing radiation are not available for most part of the Mars Express data set (until the MAVEN spacecraft mission), we use the F10.7 solar radio flux measured at Earth and recalculated to the Mars location as its proxy. The respective dependence obtained for the fit parameters α is shown in Figure 21. Each point represents a single spectral fit and the red lines represent the median values in individual 10^{-21} W m^{-2} Hz^{-1} wide intervals. The median values start at around -1.2 and then they slowly decrease down to about -1.6 for F10.7 solar radio flux interval 70-80.10^{-22} W m^{-2} Hz^{-1}.

Figure 21 - The values of α parameters of successful spectral fits as a function of the F10.7 solar radio flux recalculated to the Mars location. The horizontal red lines represent median values in individual 10-21 W m-2 Hz-1 wide intervals.

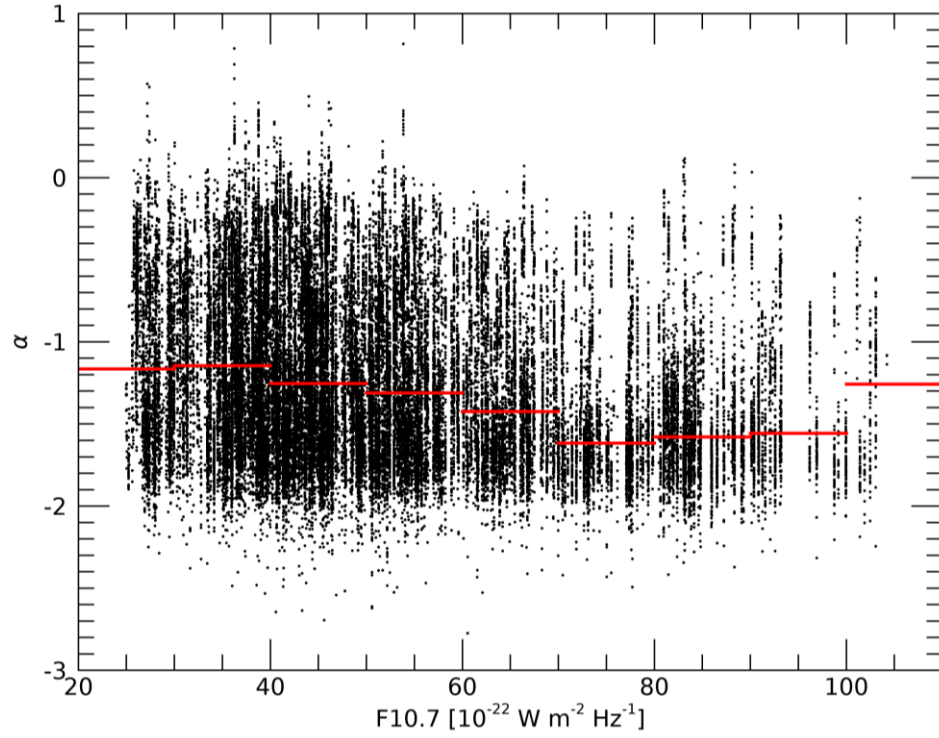**Figure 22 - The values of C_n parameters of successful spectral fits as a function of the F10.7 solar radio flux recalculated to the Mars location. The red horizontal lines represent median values in individual 10-21 W m-2 Hz-1 wide intervals.**
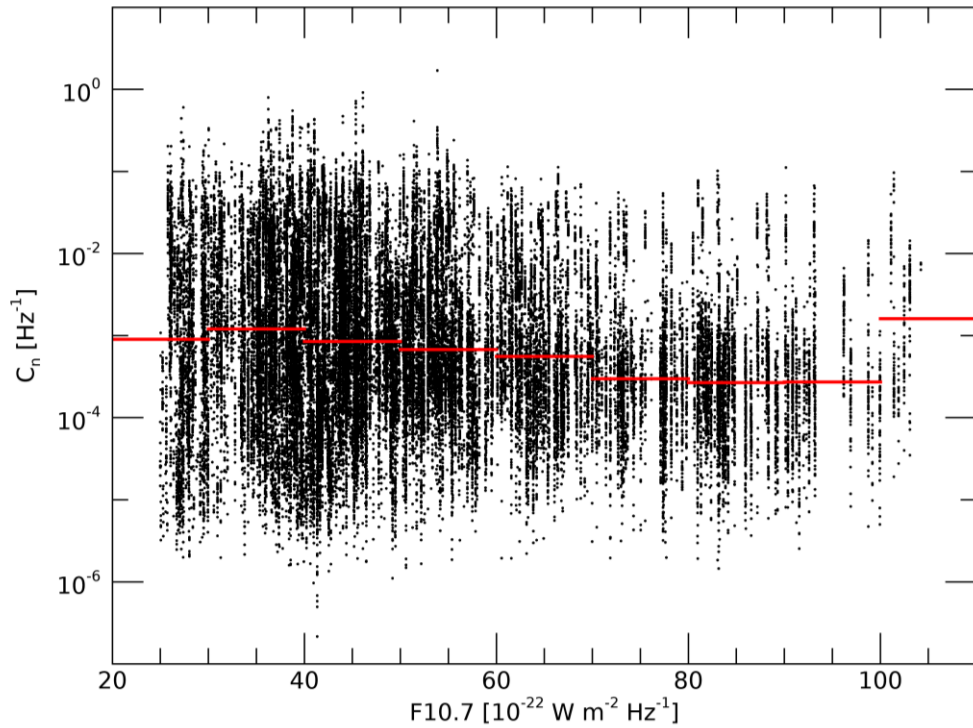
For even larger values of F10.7, the value of α remains essentially constant. Its apparent sudden increase in the highest F10.7 interval can be likely attributed to the

very low number of data points. We note that the vertical line structures apparently formed by individual data points are purely due to the sampling of the used MARSIS data.

The dependence of the spectral fit parameter C_n on the F10.7 solar radio flux recalculated to the Mars location is shown in Figure 22. Again, each dot represents a single successful spectral fit and the horizontal red lines show median values in individual 10^{-21} W m^{-2} Hz^{-1} wide intervals. The overall trend obtained for the C_n parameters is quite similar to the trend obtained for the α values.

4.3.2 Altitudinal dependence of electron density fluctuations

The altitudes 160 km, 180 km, 200 km, 220 km, 240 km, and 260 km are chosen for the calculation of the power spectra. The lowest chosen altitude essentially starts just above the peak altitude, while the highest chosen altitude roughly corresponds to the highest where the electron densities are yet available from the ionospheric sounding (not from interpolation). The altitudinal step of 20 km is deemed as sufficient to observe any systematic trends, while a finer altitudinal step would only complicate the calculation. For each electron density profile and each of the chosen altitudes, the respective electron density is used for the calculation of spectra exactly the same way as the peak electron density in the preceding section. The altitudinal dependences of the fit parameters α and C_n are then investigated.

The altitudinal dependence of the fit parameter α is shown in Figure 23. Since all the data points are grouped at the chosen discrete altitudes, their plotting would result only into apparent vertical lines in the plot and is essentially meaningless. Instead, we opt to plot the median and quartile dependences to characterize the distribution. These are shown by the red and blue lines, respectively. It can be seen that the median and quartile lines exhibit almost the same behaviour. Only at higher altitudes the quartile values slightly diverge from the median, suggesting a broader distribution of the alpha parameter. Overall, albeit a scatter in the parameter values is significant, a decreasing trend of the α parameter with altitude is observed.

The altitudinal dependence of the parameter C_n is shown in Figure 24 using the same format as in Figure 23. The quartiles again diverge more from the median value

at higher altitudes. Despite the significant scatter, the median value appears not to be monotonous; it first rises with increasing altitude, only to decrease slightly at higher altitudes.

Figure 23 - Altitudinal dependence of the α parameter. The red line shows the median dependence, and the blue lines represent 0.25 and 0.75 quartiles.
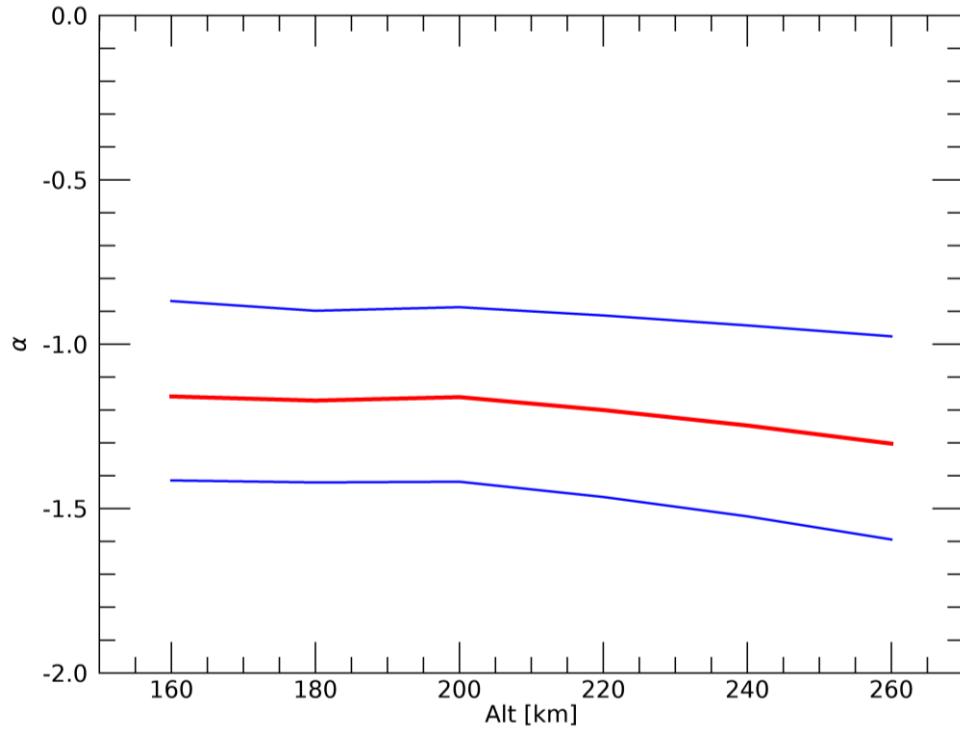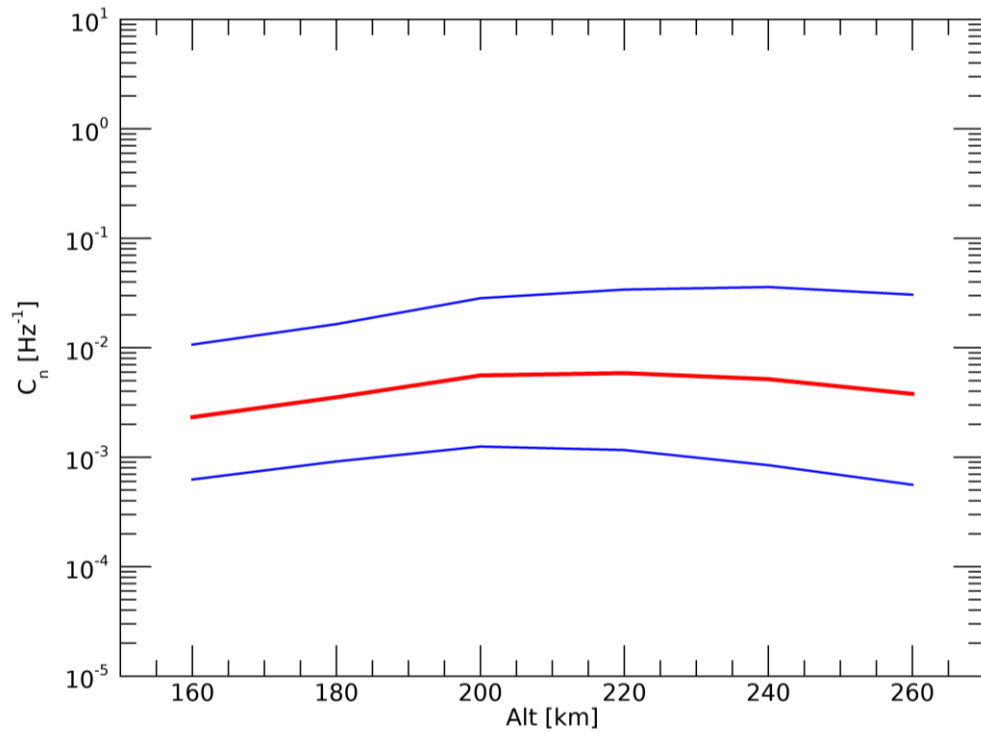

Figure 24 - Altitudinal dependence of the C_n parameter. The red line shows the median dependence, and the blue lines represent 0.25 and 0.75 quartiles.

5. Discussion

5.1 Average electron density dependences

Both the average dependences in Figure 8 and Figure 9 have a similar structure. They show the highest electron density close to the sub-solar point in accordance with equation (2). Furthermore, the electron density increases with decreasing altitude until it reaches the peak electron density. After reaching the peak electron density it should start to decrease as described by equation (1). However, this cannot be observed in Mars Express measurements, because the sounder cannot measure electron densities below the peak altitude. Furthermore, in the case of MAVEN data, there is no decrease of average density with altitude at lower altitudes at dayside (SZA < 90°). This can be explained by the MAVEN orbit usually not extending down to altitudes below the altitude of the peak electron density on the dayside, which is consistent with the expected peak altitudes in the interval of about 130-150 km, depending on SZA [24]. On the nightside, however, there are a few SZA bins where this happens. This indicates that MAVEN periodically orbits below the altitude of peak electron density on the nightside and that the peak electron density is located at higher altitudes than on the dayside.

The average electron densities depend on the magnetic field strength. Both Figure 8 and Figure 9 demonstrate that, at higher altitudes, electron densities at locations with larger magnetic field magnitudes are systematically larger than at locations with low magnetic field magnitudes. In the results obtained using the Mars Express data, the effect seems to be present even at lower altitudes on the dayside. In the results obtained using the MAVEN data, the effect at lower altitudes essentially disappears. The increase of average electron densities in regions with strong magnetic fields at higher altitudes is consistent with [33].

5.2 Deviations from the Chapman model

The applied fit conditions allow us to conveniently select the orbits with a sufficient number of data points and with the respective electron densities following well the expected Chapman dependence. For such cases, the only fit parameter according to equation (2) is the peak electron density in the sub-solar point. The obtained values of $\sim 10^5$ cm^{-3} are in agreement with expected subsolar peak electron

densities [24]. Therefore, using peak electron densities measured during a single orbit for SZA < 75° and equation (2) is a good way to find the peak electron density in the subsolar point. It also nicely demonstrates that, for given external conditions (which can be assumed to be constant during a given orbit), the Chapman theory predicts the SZA dependence of peak electron densities very accurately.

We attempted to compare the dependence of subsolar peak electron density on the solar radiation flux F10.7 for the northern and the southern hemisphere of Mars. The main motivation is that the strong crustal magnetic fields are located primarily in the southern hemisphere, while they are basically absent in the northern hemisphere. The northern/southern division might be thus another possibility how to investigate a possible controlling role of crustal magnetic fields for the ionospheric formation. However, this turned out not to be possible for the used MARSIS dataset and the Chapman fit conditions applied, because the subsolar peak electron densities calculated for the two hemispheres do not overlap in the F10.7 domain. The value 3.10^{-21} W m^{-2} Hz^{-1} of F10.7 index divides the orbits to mostly northern or mostly southern, with the mostly northern having lesser F10.7 values.

We further tried to investigate local deviations from the Chapman fits. However, these deviations from the Chapman model show mostly no or only a very weak dependence on considered outside parameters. Figure 11 and the Figure 13 reveal some indications of possible very weak dependences. Nevertheless, given the large scatter of individual data points and sampling biases present in the MARSIS data set, they are questionable at best.

5.3   Spectra of electron density fluctuations

Although power spectral densities and spectral shapes obtained for individual time intervals are quite different, they are usually well fitted by equation (9).

For all investigated dependences, the spectral slope parameter α decreases with the independent parameter, either SZA or F10.7, to lower values ultimately approaching the expected -5/3 value. Curiously, there are two rather distinct groups of spectra. The first of them corresponds to higher values of alpha and generally quite large power spectral densities, while the second of them corresponds to lower alpha

values and lower spectral densities. The distinction is particularly clear for the SZA dependences plotted in Figure 19 and Figure 20, as the difference between two groups of spectra is most pronounced for lower SZAs and it eventually nearly disappears close to the terminator. A closer inspection of the time series corresponding to the two types of spectra reveals that the spectra with larger values of α and larger power spectral densities typically contain a profile with substantially lower peak electron density. After confirming that these sudden electron density depressions are not a digitalisation error, two explanations appear plausible. A further analysis and considerations are needed to definitively solve the issue.

Firstly, the measurements might truly be correct and there is in fact an ionospheric depression or an ionospheric hole. There are reports of similar structures on the nightside of Mars and in the ionosphere of Jupiter [34, 35]. However, to the best of our knowledge, such ionospheric holes have not yet been reported in the Martian dayside ionosphere.

Secondly, there is evidence for localised structures with enhanced electron densities in the Martian ionosphere [36, 37]. Such structures might possibly result in the sounding signal incidence not perpendicular to the electron density isocontour. The MARSIS pulse might then be reflected in a different direction than where it came from, and the reflection would not be registered. The MARSIS ionogram would then lack some of the higher electron density readings. With the higher density readings missing, the lower electron density readings are incorrectly interpreted as peak electron densities, resulting in sudden depressions observed in the data.

The values of the α parameter tend to decrease with increasing altitude, but they remain higher than the expected value of -5/3 all over the analysed altitudinal range. This can be again likely explained in terms of the ionospheric depressions, which result in higher α parameter values than other time series. On the other hand, the altitudinal dependence of the value of the parameter C_n is not monotonous. Although the scatter of the values is large, the median C_n values tend to increase with altitude up to about 220 km, while they tend to decrease with altitude at higher altitudes. This behaviour at the higher altitudes seems to contradict former studies, which reported the relative amplitude of the fluctuations to increase with altitude [17]. It can be, however, likely explained by the limitations of the MARSIS radar sounding

data used in the present study. Considering the low power of the sounding signal at low frequencies and the related lower limit on electron densities detectable by the ionospheric sounding, most of the electron density profiles at altitudes higher than 220 km are based on the interpolation employed in the trace inversion routine rather than on the radar sounding measurements themselves. This interpolation necessarily results in an electron density profile smoothing and a suppression of electron density fluctuations at these altitudes.

Conclusion

In the first part, we studied the dependences of average electron densities on the selected controlling parameters. We showed that the overall behaviour of average electron densities corresponds to the Chapman model and that electron densities at higher altitudes are significantly enhanced in regions with strong crustal magnetic fields. Moreover, quite importantly, the results based on the Mars Express and the MAVEN spacecraft data are essentially the same, demonstrating the consistency between these two independent data sets.

In the second part, we showed that the peak electron density in the subsolar point can be determined by fitting peak electron densities measured by Mars Express during a single orbit by a Chapman-predicted SZA dependence. Limiting the analysis to not too large SZAs, it is possible to approximate the Chapman grazing incidence function simply by sec(SZA). We analysed deviations of peak electron densities from this fit and their possible dependences on outside controlling parameters.

In the last part, we studied frequency spectra of the fluctuations of peak electron densities in the Martian ionosphere as a function of outside factors. The spectra can be successfully fitted by a power law dependence, and each spectrum is thus characterized by only two fit parameters. They are found to systematically vary with SZA and F10.7. Moreover, we identified two distinct types of frequency spectra. This is explained in terms of localised sudden significant electron density drops present in some of the time series, resulting in higher spectral power and more flat spectra. The precise nature of these measurements is not known and requires further study.

Bibliography

1.   SÁNCHEZ-CANO, B., HERRAIZ, M., RODRÍGUEZ-CADEROT, G., et al. Study of the ionosphere of Mars: application and limitations of the Chapman-layer model. *Highlights of Spanish Astrophysics VI, Proceedings of the IX Scientific Meeting of the Spanish Astronomical Society*. 2010. P. 442–453.

2.   LUHMANN, J.G. *Introduction to Space Physics*. Cambridge : Press Syndicate of the University of Cambridge, 1995.

3.   TROTIGNON, J. G., PARROT, M., CERISIER, J. C., et al. The plasma environment of Mars: from the shocked solar wind down to the ionosphere. *Planetary and Space Science*. 2000. Vol. 48, no. 12–14, p. 1181–1191. DOI 10.1016/s0032-0633(00)00102-1.

4.   ACUÑA, M. H., CONNERNEY, J. E.P., WASILEWSKI, P., et al. Magnetic field and plasma observations at Mars: Initial results of the Mars global surveyor mission. *Science*. 1998. Vol. 279, no. 5357, p. 1676–1680. DOI 10.1126/science.279.5357.1676.

5.   ACUÑA, M. H., CONNERNEY, J. E.P., NESS, N. F., et al. Global distribution of crustal magnetization discovered by the Mars Global Surveyor MAG/ER experiment. *Science*. 1999. Vol. 284, no. 5415, p. 790–793. DOI 10.1126/science.284.5415.790.

6.   NĚMEC, F., LINZMAYER, V., NĚMEČEK, Z., et al. Martian Bow Shock and Magnetic Pileup Boundary Models Based on an Automated Region Identification. *Journal of Geophysical Research: Space Physics*. 2020. Vol. 125, no. 11, p. 1–16. DOI 10.1029/2020JA028509.

7.   DIEVAL, Catherine. *Solar Wind Ions Inside the Induced Magnetosphere of Mars*. Luleå University of Technology, 2012.

8.   MCELROY, M. B., KONG, T. Y., YUNG, Y. L., et al. Composition and Structure of the Martian Upper Atmosphere: Analysis of Results from Viking. *Science*. 1976. Vol. 194, no. 4271, p. 1295–1298. DOI 10.1126/science.194.4271.1295.

9. WITHERS, Paul. A review of observed variability in the dayside ionosphere of Mars. *Advances in Space Research*. 2009. Vol. 44, no. 3, p. 277–307. DOI 10.1016/j.asr.2009.04.027.

10. SCHUNK, Robert W. and NAGY, Andrew F. *Ionospheres*. Cambridge University Press, 2000.

11. FOX, J. L. and YEAGER, Katherine E. Morphology of the near-terminator Martian ionosphere: A comparison of models and data. *Journal of Geophysical Research*. 2006. Vol. 111, no. A10, p. A10309. DOI 10.1029/2006JA011697.

12. CHAPMAN, S. The absorption and dissociative or ionizing effect of monochromatic radiation in an atmosphere on a rotating Earth. *Proceedings of the Physical Society*. 1931. Vol. 43, no. 1, p. 26–45. DOI 10.1088/0959-5309/43/1/305.

13. MARTINIS, Carlos R. Modeling day-to-day ionospheric variability on Mars. *Journal of Geophysical Research*. 2003. Vol. 108, no. A10, p. 1383. DOI 10.1029/2003JA009973.

14. NĚMEC, F., MORGAN, D. D., GURNETT, D. A., et al. Nightside ionosphere of Mars: Radar soundings by the Mars Express spacecraft. *Journal of Geophysical Research E: Planets*. 2010. Vol. 115, no. 12, p. 1–9. DOI 10.1029/2010JE003663.

15. NĚMEC, F., MORGAN, D. D., GURNETT, D. A., et al. Areas of enhanced ionization in the deep nightside ionosphere of Mars. *Journal of Geophysical Research E: Planets*. 2011. Vol. 116, no. 6, p. 1–9. DOI 10.1029/2011JE003804.

16. DALY, PATRICK W; PASCHMANN, Gotz. *Analysis Methods for Multi-Spacecraft Data*. Bern, 2000.

17. GURNETT, D. A., MORGAN, D. D., DURU, F., et al. Large density fluctuations in the martian ionosphere as observed by the Mars Express radar sounder. *Icarus*. 2010. Vol. 206, no. 1, p. 83–94.

DOI 10.1016/j.icarus.2009.02.019.

18. KOLMOGOROV, A N. *The Local Structure of Turbulence in Incompressible Viscous Fluid for Very Large Reynolds Numbers*. 1991.

19. DURU, F., GURNETT, D. A., MORGAN, D. D., et al. Electron densities in the upper ionosphere of Mars from the excitation of electron plasma oscillations. *Journal of Geophysical Research: Space Physics*. 2008. Vol. 113, no. 7, p. 1–15. DOI 10.1029/2008JA013073.

20. TAPPING, K. F. The 10.7 cm solar radio flux (F10.7). *Space Weather*. 2013. Vol. 11, no. 7, p. 394–406. DOI 10.1002/swe.20064.

21. NĚMEC, F., MORGAN, D. D., KOPF, A. J., et al. Characterizing Average Electron Densities in the Martian Dayside Upper Ionosphere. *Journal of Geophysical Research: Planets*. 2019. Vol. 124, no. 1, p. 76–93. DOI 10.1029/2018JE005849.

22. CHICARRO, A., MARTIN, P., & TRAUTNER, R. The Mars Express mission: an overview. *Mars Express: the scientific payload.* 2004. P. 3–13.

23. GURNETT, D. A., KIRCHNER, D. L., HUFF, R. L., et al. Radar Soundings of the Ionosphere of Mars. *Science.* 2005. Vol. 310, no. 5756, p. 1929–1933. DOI 10.1126/science.1121868.

24. GURNETT, D. A., HUFF, R. L., MORGAN, D. D., et al. An overview of radar soundings of the martian ionosphere from the Mars Express spacecraft. *Advances in Space Research*. 2008. Vol. 41, no. 9, p. 1335–1346. DOI 10.1016/j.asr.2007.01.062.

25. JORDAN, R., PICARDI, G., PLAUT, J., et al. The Mars express MARSIS sounder instrument. *Planetary and Space Science*. 2009. Vol. 57, no. 14–15, p. 1975–1986. DOI 10.1016/j.pss.2009.09.016.

26. JAKOSKY, B. M., LIN, R. P., GREBOWSKY, J. M., et al. The Mars Atmosphere and Volatile Evolution (MAVEN) Mission. *Space Science Reviews*. 2015. Vol. 195, no. 1–4, p. 3–48. DOI 10.1007/s11214-015-0139-x.

27. ANDERSSON, L., ERGUN, R. E., DELORY, G. T., et al. The langmuir probe and waves (LPW) instrument for MAVEN. *Space Science Reviews*. 2015. Vol. 195, no. 1–4, p. 173–198. DOI 10.1007/s11214-015-0194-3.

28. DELORY, G T, ANDERSSON, L, ERGUN, R E, et al. Design and Performance of the Langmuir Probe on the MAVEN Mission. In : *46th Lunar and Planetary Science Conference*. 2015.

29. MORGAN, D. D., WITASSE, O., NIELSEN, E., et al. The processing of electron density profiles from the Mars Express MARSIS topside sounder. *Radio Science*. 1 May 2013. Vol. 48, no. 3, p. 197–207. DOI 10.1002/rds.20023.

30. NĚMEC, F., MORGAN, D D and GURNETT, D A. On improving the accuracy of electron density profiles obtained at high altitudes by the ionospheric sounder on the Mars Express spacecraft. *Journal of Geophysical Research: Space Physics*. 2016. Vol. 121, no. 10, p. 10,117-10,129. DOI 10.1002/2016JA023054.

31. NĚMEC, F., MORGAN, D D, FOWLER, C M, et al. Ionospheric Electron Densities at Mars: Comparison of Mars Express Ionospheric Sounding and MAVEN Local Measurements. *Journal of Geophysical Research: Space Physics*. 2017. Vol. 122, no. 12, p. 12393–12405. DOI 10.1002/2017JA024629.

32. CAIN, Joseph C., FERGUSON, Bruce B. and MOZZONI, David. An n = 90 internal potential function of the Martian crustal magnetic field. *Journal of Geophysical Research E: Planets*. 2003. Vol. 108, no. 2, p. 1–19. DOI 10.1029/2000je001487.

33. NĚMEC, F., MORGAN, D D, GURNETT, D A, et al. Empirical model of the Martian dayside ionosphere: Effects of crustal magnetic fields and solar ionizing flux at higher altitudes. *Journal of Geophysical Research A: Space Physics*. 2016. Vol. 121, no. 2, p. 1760–1771. DOI 10.1002/2015JA022060.

34. DURU, F., GURNETT, D. A., MORGAN, D. D., et al. Nightside ionosphere of Mars studied with local electron densities: A general overview and electron

density depressions. *Journal of Geophysical Research: Space Physics*. 2011. Vol. 116, no. A10, p. n/a-n/a. DOI 10.1029/2011JA016835.

35.   IMAI, Masafumi, KOLMAŠOVÁ, Ivana, KURTH, William S., et al. Evidence for low density holes in Jupiter's ionosphere. *Nature Communications*. 2019. Vol. 10, no. 1, p. 6–11. DOI 10.1038/s41467-019-10708-w.

36.   NĚMEC, F., ANDREWS, D. J., MORGAN, D. D., et al. Oblique Reflections of Mars Express MARSIS Radar Signals From Ionospheric Density Structures: Raytracing Analysis. *Journal of Geophysical Research: Planets*. 2019. Vol. 124, no. 5, p. 1177–1187. DOI 10.1029/2018JE005891.

37.   DURU, F., GURNETT, D. A., AVERKAMP, T. F., et al. Magnetically controlled structures in the ionosphere of Mars. *Journal of Geophysical Research: Space Physics*. 2006. Vol. 111, no. 12, p. 1–6. DOI 10.1029/2006JA011975.

List of Abbreviations

DFT - Discrete Fourier transform

EUV - Extreme ultraviolet

FT - Fourier transform

IMF - Interplanetary magnetic field

LP – Langmuir Probe

LPW - Langmuir Probe and Waves

MARSIS - Mars Advanced Radar for Subsurface and Ionosphere Sounding

MAVEN - Mars Atmosphere and Volatile EvolutioN

MBP - Magnetic pile-up boundary

MGS - Mars Global Surveyor

PSD - Power spectral density

SZA - Solar Zenith Angle

WFT - Windowed Fourier transform